Nanoscale

Harvesting Resonantly-Trapped Light for Small Molecule Oxidation Reactions at the Au/α-Fe_2O_3 Interface

Journal:	*Nanoscale*
Manuscript ID	NR-ART-02-2018-001330.R1
Article Type:	Paper
Date Submitted by the Author:	22-Mar-2018
Complete List of Authors:	McClure, Joshua; US Army Research Laboratory, ; Grew, Kyle; US Army Research Laboratory Baker, David; U.S. Army Research Laboratory, Sensors and Electron Devices Directorate Das, Naresh; US Army Research Laboratory, Chu, Deryn; US Army Research Laboratory, Sensors and Electron Devices Directorate Gobrogge, Eric; US Army Research Laboratory

Harvesting Resonantly-Trapped Light for Small Molecule Oxidation Reactions at the Au/α-Fe_2O_3 Interface

Joshua P. McClure, Kyle N. Grew, David R. Baker, Eric Gobrogge, Naresh Das and Deryn Chu

[1]U.S. Army Research Laboratory, Adelphi, MD, 2800 Powder Mill Road, Adelphi, MD 20783, U.S.A.

ABSTRACT

Plasmonic metal nanoparticles (NPs) extend the overall light absorption of semiconductor materials. However, it is not well understood how coupling metal NPs to semiconductors alters the photo-electrochemical activity of small molecule oxidation (SMO) reactions. Different photo-anode electrodes comprised of Au NPs and α-Fe_2O_3 are designed to elucidate how the coupling plays not only a role in the water oxidation reaction (WO) but also performs for different SMO reactions. In this regard, Au NPs are inserted at specific regions within and/or on α-Fe_2O_3 layers created with a sequential electron beam evaporation method and multiple annealing treatments. The SMO and WO reactions are probed with broad-spectrum irradiation experiments with an emphasis on light-driven enhancements above and below the α-Fe_2O_3 band gap. Thin films of α-Fe_2O_3 supported on a gold back reflective layer resonantly-traps incident light leading to enhanced SMO/WO conversion efficiencies at high overpotential (η) for above band-gap excitations with no SMO activity observed at low η. In contrast, a substantial increase in the light-driven SMO activity is observed at low η, as well as for below band-gap excitations when sufficiently thin α-Fe_2O_3 films are decorated with Au NPs at the solution-electrode

interface. The enhanced photo-catalytic activity is correlated with increased hydroxyl groups at the Au/α-Fe_2O_3 interface, as well as simulated volume-integrated near-field enhancements over select regions of the Au/α-Fe_2O_3 interface providing an important platform for future SMO/WO photo-electrocatalyst development.

INTRODUCTION

The complete electrochemical oxidation of alcohol fuels containing a single carbon-carbon (i.e., C-C) bond such as ethanol is difficult to perform at low temperatures (i.e, < 80°C). It is well known that at these low temperatures alcohols containing C-C bonds are not completely dissociated due to inefficient catalyst activation.[1] As a result, state-of-the-art electrochemical power generators typically use fuels that don't contain C-C bonds (e.g., methanol, formic acid, H_2, N_2H_4, etc.), or perform high-temperature catalytic reformation steps. However, these approaches are not optimal for portable systems since fuels without C-C bonds have either a lower specific energy (e.g., methanol is lower than ethanol and ethylene glycol on a kW kg^{-1} basis) or are considered unsafe (e.g., hydrazine, N_2H_4). Moreover, reformation components increase the system complexity and weight required, thereby lowering the overall specific energy density of the device.[2] Several strategies have been undertaken to facilitate small molecule oxidation (SMO) at low temperatures including Pt- or Pd-alloying[3-5], metal-oxide promotion (i.e., metal in combination with TiO_2, Sn-doped TiO_2, CeO_2, Ce-doped α-MoO_3, ZrO_2 etc.)[6-10], altering the nanoparticle aspect ratio and geometry (e.g., core-shell, rods, antennas, etc.)[11-13] and modifying the reaction media[14-15]. In addition to these strategies, integrating plasmonic metal nanoparticles (NPs) into electrodes creates many opportunities. Once plasmonic NPs are integrated into the electrode the redox kinetics and selectivity of the

desired SMO reaction can be enhanced or altered with light-driven processes in conjunction with an anodic bias.[16-18] Plasmonic-enhancement was previously demonstrated for gold nanofiber electrodes with observed photo-enhancements for both the methanol and ethanol oxidation reactions.[19] In addition to plasmonic metals, coupling metallic NPs with a semiconductor structure extends the photo-catalytic devices' absorption of the available solar spectrum, thereby increasing the energy available to promote oxidation.[20-22]

Metal-semiconductor photo-active electrodes have been demonstrated in various energy-related applications including water-splitting[23-25], carbon dioxide reduction[26], hydrogen dissociation[27], formic acid oxidation[28-29], among other findings. For example, metal-semiconductor electrodes that utilize metal NPs as light antennas to transfer energy to the adjacent semiconductor has been shown to enhance photo-conversion in the adjacent semiconductor both above and below the band gap.[30] It was previously reported that positioning NPs at different locations within a film and/or incorporating a metal reflector allows one to reduce the physical thickness of the semiconductor.[25, 31] Therefore, efficient hot carrier extraction is possible for metal-semiconductor-metal (MSM) and metal-insulator-metal (MIM) systems with optimally configured back reflector contacts and semiconductor thicknesses.[32-33] Despite successful demonstrations, incorporating plasmonic metal NPs into an electrode without optimization of the materials, the electrode configuration and the light trapping scheme often leads to a decreased light-driven performance.

We describe different Au/α-Fe_2O_3 electrode configurations for SMO reactions at low overpotentials (η) and compare the performance to the water oxidation (WO) reaction and mixed SMO/WO reactions at high η. Au NPs are of particular interest since they exhibit extinction cross sections up to 10× their geometrical cross-section,[34] are chemically stable and

electrochemically active in alkaline media,[35-36] and have shown increased electrochemical activities with decreasing NP size.[37] In addition, α-Fe_2O_3 is chemically stable in high pH media, readily abundant, absorbs solar irradiation due to a desirably situated band-gap, and exhibits spectral overlap with Au NPs near the band-edge.[38] It was previously shown that porous α-Fe_2O_3 decorated with Au NPs were effective ethanol gas sensing substrates.[39] In addition, interface manipulation of α-Fe_2O_3 with Au NPs and/or Al_2O_3 was shown to be an effective strategy to promote plasmon-coupled water-splitting.[40] However, a thorough undertaking of photo-enhanced SMO reactions has not been established. The ultimate objective is to configure the metal-semiconductor architecture to efficiently extract electrons while promoting the migration of holes to the solution-electrode interface. It remains unclear how positioning Au NPs at the surface and/or within a semiconductor effects the overall charge-transfer dynamics for SMO electrocatalytic reactions. The results highlight important design considerations and quantify the potential-dependent light-driven SMO and WO reaction responses.

EXPERIMENTAL

Electron-Beam Evaporation

Thin film (TF), surface (SF), embedded (EM) and distributed (DB) structures were fabricated using a sequential electron-beam evaporation process. All electrodes were prepared on pre-cleaned fluorine-doped SnO_2 (FTO) substrates (i.e., 500 μm thickness with a 9 Ω-cm^2 resistance). Depositions were performed in an Evatec BAK 641 electron-beam (EB) evaporation tool with a base pressure of ~10^{-6}-10^{-7} Torr and a collector rotation rate of 15 rpm. The total deposited sample thickness was monitored via a quartz crystal with a targeted deposition rate of 0.2 and 0.3 nm s^{-1} for Fe_xO_y and Au materials, respectively. Three different Fe_xO_y nominal

thicknesses were considered (i.e., 25, 50 and 75 nm) for the TF, SF, EM and DB electrodes resulting in twelve different wafer-size electrode configurations. The sample thicknesses were determined for the α-Fe_2O_3 and Au layer depositions independently on control Si double-side polish wafers by measuring the step height profile with a KLA Tencor P-15 profilometer. The step-height profiles were calibrated with Tencor step-height control samples. The Si control wafers minimized surface roughness effects commonly observed for FTO substrates and allowed accurate determination of the deposit thickness for determining the tooling factor and subsequent deposition rate. The measured iron oxide thicknesses are 27.2 ± 2.3 nm, 51.7 ± 3.1 nm, and 77.1 ± 1.5 nm. The iron oxide thicknesses reported here-in are nominal values for simplicity. For all electrodes discussed, a 50 nm layer of Au (Au Layer 1) was deposited on FTO to serve as a working electrode contact, as well as a back metal reflector for light-trapping. The back contact (Au Layer 1) thickness is 51.4 ± 3.3 nm measured by profilometry. A schematic of the EB deposition steps (i.e., EB1, EB2, EB3), as well as annealing (ΔT) treatments is shown in Fig. 1. The TF electrodes were prepared by depositing iron oxide (Fe_xO_y) on the Au film-coated FTO followed by annealing (ΔT) in a Tystar tube furnace; the specifics of the annealing steps are outlined in the next experimental subsection. The SF configurations were prepared similarly to the TF samples; however, a 5-nm Au film was added to the surface of the Fe_xO_y before annealing (EB1 followed by ΔT). The EM and DB configurations required two annealing steps to achieve Au NPs at an embedded and/or surface location. Specifically, the EM configuration was prepared by adding Au NPs at the midpoint in the nominal 25, 50 or 75 nm Fe_xO_y thin film. For example, for the nominal 50-nm thin Fe_2O_3 film, Au NPs were added to the surface of 25 nm of Fe_xO_y followed by an additional coating layer of 25 nm of Fe_xO_y, which encased the Au NPs (EB2 followed by ΔT). The DB configurations were developed by adding Au NPs at the

midpoint of the Fe_xO_y film, as well as at the surface (EB3 followed by ΔT). It is worth noting, that only the location of the Au NPs was altered for each configuration to effectively normalize the iron oxide mass loadings for the TF, SF, EM and DB configurations.

Single- or Multi-Step Annealing

The annealing procedure (i.e., ΔT for each step previously discussed in the EB section) is an important process for creating the TF, SF, EM and DB electrodes. First, 100 mm FTO wafers coated with sample were loaded into quartz trays and introduced from room temperature into a Tystar tube furnace preheated to 350°C at a controlled speed, which allowed the sample to slowly equilibrate to the initial tube furnace temperature. The sample-loaded tube furnace was then ramped from 350°C to 450°C at 2°C min^{-1} in N_2 with 200 sccm of O_2. Next, the temperature of the furnace was held at 450°C for 4 hr and the N_2 flow-rate was simultaneously reduced until there was only a pure O_2 gas flow. The pure O_2 environment and length of annealing converts the evaporated iron oxide (i.e., denoted as Fe_xO_y) to α-Fe_2O_3. The pure O_2 environment and annealing time also simultaneously converted the thin 5 nm Au film to NPs. Next, the furnace temperature was ramped down at 2°C min^{-1} to 350°C in a mixed N_2/O_2 atmosphere and slowly removed at room temperature.

Photo-Electrochemical Experiments

The TF, SF, EM and DB electrodes were studied in two different custom-made Teflon apparatuses. Figure S1 shows the two different apparatuses used for the photo-electrochemical experiments excited with a continuous wave laser (CWL) and solar-simulated light experiments (AM1.5G). The power densities for the CWL and AM1.5G experiments were calibrated using a

photo-diode in place of a typical working electrode. The power densities for the CWL experiments were controlled from ~5-70 mW cm^{-2} (i.e., a typical power density range for both λ = 532 and 785 nm). The power density for the AM1.5G experiments was calibrated to ~100 mW cm^{-2} at the location of the sample for the custom-built apparatus. The power decreased with the insertion of cut-off filters in-line with the light path. The power and current densities for a given experiment (i.e., at a given voltage), were used to convert to incident-photon-to-current efficiencies (IPCE %) with the following equation:

$$\text{IPCE \%} = 100\times \frac{I(A\ cm^{-2})}{P(W\ cm^{-2})} \times \frac{1240}{\lambda(nm)} \qquad [1]$$

Both three-electrode cells were fitted with an O-ring to set the geometric areas to 0.61 and 0.99 cm^{-2} for the CWL and AM1.5G experiments, respectively. Based on the geometric electrode areas and assuming a density of 5.25 g cm^{-3} and 19.32 g cm^{-3} for iron oxide and Au, respectively, the final mass loadings of the Au Layer 1, and three different iron oxide layers (i.e., correlated to the three different thicknesses measured by profilometry) are 58.9 ± 3.9, 8.7 ± 0.7, 16.5 ± 1.0, 24.7 ± 0.5 μg cm^{-2} for the CWL experiments. For the AM1.5G experiments, the mass loadings of the Au Layer 1 and three different iron oxide layers are 95.6 ± 6.3, 14.1 ± 1.18, 26.8 ± 1.59, 40.07 ± 0.8 μg cm^{-2}, respectively. The Au NP loading is based on a 5 nm nominal thickness and yielded approximately 5.9 and 9.6 μg cm^{-2} for the CWL and AM1.5G experiments, respectively. To achieve the optimal photo-electrochemical response for the CWL experiments, the objective was set to 5× for an experimentally optimized cell distance, with the laser excitation incident through a sapphire window. For the AM1.5G experiments, the light housing was equipped with a 300 W Xe bulb, an AM1.5G filter, and select cut-off filters (LPF) as appropriate. Both apparatuses included a Pt coil counter and reference (i.e., Ag/AgCl, Sat. KCl) electrodes, which along with the fabricated TF, SF, EM and DB working electrodes were

connected to a Gamry potentiostat for photo-electrochemical experiments. All electrochemical experiments were performed at room temperature in high pH media (0.1M KOH) with and without the presence of either 0.5M Methanol (MeOH), Ethanol (EtOH) or Ethylene Glycol (EG). Solutions were sparged with N_2 prior to testing, and a continuous stream of N_2 flowed in the head-space through a built-in port. The potentials reported were converted to the reference hydrogen electrode (RHE) scale with the following formula:

$$E_{RHE} = E_{Ag/AgCl} + 0.0596\times\text{pH} + E^0_{Ag/AgCl} \qquad [2]$$

where $E_{Ag/AgCl}$ is the measured potential, $E^0_{Ag/AgCl}$ is 0.197 V, and a nominal pH of 13. For select chronoamperometry and photo-potential experiments, the results were background subtracted to decouple the light-driven response from the dark response (i.e., absence of illumination). Examples of the background subtraction method used for chronoamperometric experiments and open-circuit potential experiments are shown in Figures S5 and S7.

X-Ray Photoelectron Spectroscopy

X-ray photo-electron spectroscopy (XPS) measurements were performed on a ULVAC PHI VersaProbe III with monochromatic Al Kα source energy of 1486.6 eV. The spot size for X-rays was 100 μm with an X-ray power of 25W. The pass energy was set to 224 eV and 55 eV for surveys and high-resolution scans, respectively. The high-resolution and survey scans were shifted to align the adventitious C1s peak at 284.8 eV. High-resolution spectra were fitted using Casa XPS software with a Shirley background and each peak-fit component line-shape set to GL(30) for the O1s spectra.

Diffuse Reflectance Spectroscopy

The UV-Vis transmittance and diffuse reflectance was measured with an Avaspec 2048 spectrophotometer and halogen light source. Diffuse reflectance (%R) measurements were collected with an Avasphere-30 PTFE integrating sphere with data collection set to a 250 ms integration time with averaging over 100 scans. The transmittance (%T) was also collected with the same Avantes setup without the need for the integrating sphere and setting the integration time to 4 ms with averaging over 250 scans. Both spectra were acquired after subtracting the underlying FTO substrate with the final quantity reported as Φ_{Abs} = 1-T-R (%).

Atomic Force and Scanning Electrochemical Microscopy.

Atomic force microscopy (AFM) was performed in ACAFM mode (164.2 kHz) on an Agilent AFM (Model 5500, Keysight Technologies) using 150 kHz Silicon probes with a DLC coated tip (Ted Pella, Inc.). Data was collected using Agilent's Pico-View software over a 5 μm x 5 μm area, and scans were collected at 6.125 μm s^{-1}. Gwyddion freeware was used to visualize all images. Scanning electron microscope (SEM) images were obtained with a Zeiss Auriga 60 Field-Emission SEM. Additional SEM images with energy dispersive spectroscopy (SEM-EDS) were acquired using a XEIA field-emission gun SEM. The TF, SF, EM and DB electrodes were imaged for all Fe_2O_3 loadings, and were typically inspected at 2-5 kV, with a working distance of ~5 mm, and the stage at either 0° or 15° tilt. Image J software was used to measure Au NP distributions, as well as α-Fe_2O_3/Au Layer 1/FTO substrate sizes for each electrode configuration.

HAADF-STEM, TEM & EDS Imaging

Cross-sections were prepared using focused ion beam SEM (FIB-SEM). First the sample was coated with carbon for ~4 sec. with an estimated thickness of 20 nm to protect the surface of the Au/α-Fe_2O_3 samples. Next, an area of 750 μm^3 was coated with Pt using a 30 kV Xe ion beam at 150 pA for 30 mins (Tescan XEIA). The cross-section lamellae were prepared with a 30kV Ga+ ion beam at 145 pA, and then was subsequently polished at 2 kV and 45 pA (Tescan GAIA). High-resolution transmission electron microscopy (TEM) and high angle annular dark-field scanning transmission electron microscopy (HAADF-STEM) of the Au/α-Fe_2O_3 samples was performed using a JEOL JEM-2100 (FEG-TEM). The accelerating voltage was maintained at 200 kV with probe size of 0.5 nm for STEM-HAADF imaging and an inner/outer collection angle of 80 and 200 mrad for EDS measurements, respectively.

Discrete Dipole Approximation Simulations

The discrete dipole approximation (DDA) methodology was used to perform electromagnetic scattering simulations in this study.[41-43] DDSCat, which employs the DDA methodology, has been used to discretize target structures as a system of finite sized dipoles, subject to electromagnetic radiation at a prescribed wavelength. This methodology uses the Clausius-Mossotti relations to account for the effects of material (dipole) polarization on local relative dielectric. Both the near-field and far-field electromagnetic scattering characteristics were calculated with the DDA methodology. For each electrode configuration examined within the current work, a doubly-periodic system was created, discretized and analyzed. The resulting (far-field) scattering characteristics were extracted from the Mueller scattering intensity matrix.[41] In addition, the near-field enhancements that take the form of local electric fields were also calculated with this methodology. In order to provide a more systematic and quantitative

measure of the influence of the structure materials and geometry on the near-field scattering, volume-normalized integrations of the square of the near field enhancement (i.e., square of the ratio of the local and incident electric fields and denoted ρ(λ,φ)) were additionally performed.[43] The ρ(λ,φ) was determined using the following equation:

$$\rho(\lambda,\varphi) = \frac{1}{V_\varphi}\int_V \left|\frac{E}{E_0}\right|^2 dV_\varphi \qquad [3]$$

where λ, φ, $|E/E_0|^2$ are the wavelength, phase, and near-field enhancement, respectively. Additional details and discussion regarding the DDA simulations is given in the supporting information.

RESULTS & DISCUSSION

The electrode configurations were created using a sequential deposition method followed by single or multiple annealing steps. Figure 1 shows the TF, EM, SF and DB configuration schematics (dashed boxes). All configurations were created with a gold backing layer, which served as a working electrode contact, reflective layer and as a diffusion barrier to prevent doping of the iron oxide by the underlying FTO substrate.[44] After annealing, the underlying Au layer is modified and shows a decreased reflectance at λ ≥ 600 nm, which is typically observed for thermally-treated Au films.[45-46] Figure 2 shows representative SEM images of four different configurations for select iron oxide thicknesses. Figure 2a is a low and high (inset) magnification image of the TF configuration with a nominal deposited iron oxide thickness of 25 nm. Complimentary schematics of the photo-electrode configurations are shown in Fig. S2 corresponding to the SEM images in Fig. 2. After annealing, the iron oxide layer is at the surface with continuous film, and a substrate (α-Fe_2O_3/Au Layer 1/FTO) diameter size distribution centered at ~206 nm (Fig. S3). The substrate diameter distribution is mainly affected

by the FTO underlayer. This is confirmed by measuring the AFM roughness as shown in Fig. S3 and compared for similar samples. Additional Si wafer samples were prepared for comparison and exhibited a lower roughness. Raman analysis of the Fe_xO_y film before annealing has peaks characteristic of Fe_3O_4, however after annealing the Fe_3O_4 peaks disappear and the α-Fe_2O_3 phase is identified as shown in Fig. S4a. The Raman peak locations and relative peak magnitudes are consistent with previous analysis of Au/α-Fe_2O_3 composites and localized spin-waves.[47-48] Figure 2b shows after annealing Au NPs distributed across the surface of the nominal 25 nm α-Fe_2O_3 thin film (SF25). The Au NPs are uniformly dispersed with a diameter centered at ~30 ± 8 nm as shown in Fig. S3. The thin Au film conversion to Au NPs has been previously observed for thermally-treated Au films.[46, 49] Figures 2c-d show the embedded and distributed configurations for a total 50 nm α-Fe_2O_3 thickness denoted EM50 and DB50, respectively. The EM50 and DB50 configurations preserve the Au NP geometry even after the Fe_xO_y over-coating and subsequent annealing to α-Fe_2O_3. Complimentary AFM images were acquired for the different electrode configurations and are shown in Figs. S3c-f for the nominal 25 nm α-Fe_2O_3 thickness. The AFM z-height profile is similar for the different SF, TF, EM and DB configurations over the 25 μm^2 area measured. In addition to the morphological and phase identification analysis, it was necessary to determine if the α-Fe_2O_3 *successfully* over-coated the Au backing layer and/or the Au NPs positioned at the surface. Therefore, FIB-SEM cross-section lamella of the Au/α-Fe_2O_3 electrode were prepared and imaged with TEM, HAADF-STEM ad EDS mapping. Figure 3a shows a cross-section image of the EM50 sample. The EM50 sample shows the (Au Layer 1) with a thickness of ~51 nm consistent with the profilometry measurements discussed in the experimental section. In addition, multiple cross-section images confirm the ~25 nm α-Fe_2O_3 layer atop the (Au Layer 1), as well as Au NP of

~30 nm in diameter. Finally, an additional ~25 nm α-Fe_2O_3 atop the Au NPs is also observed. Figure 3b shows HAADF-STEM image over several micrometers, with EDS mapping shown in Fig. 3c. Figure 3c clearly shows the Sn (i.e., from the FTO substrate), Au (i.e., from Au Layer 1) and Fe (i.e., from the Au/α-Fe_2O_3 layer) with a continuous profile observed for the Au and Fe layers. The continuous profile and height distribution is consistent with that found from the AFM images shown in Fig. S3. Complimentary SEM-EDS images are shown in Fig. 3d for a large area with the increased Au L signal due to the Au backing layer and Au NPs. Additionally, XPS probed the surface oxygen, gold, iron surface chemistry for each configuration.

Figure 4a shows the XPS survey scans for all TF configurations considered. There is a noticeable Fe2p, O1s, and Fe3p signature associated with the iron oxide layer. High resolution spectra of the Fe2p binding energy region (Fig. S4b) show the $Fe2p_{3/2}$ peak approximately centered at ~711 eV, which suggests a Fe^{3+} oxidation state.[44, 50] For the TF25, TF50 and TF75 samples the $Fe2p_{3/2}$ peak is approximately centered at 710.6 ± 0.03 eV. For the SF25, TF50 and TF75 samples, the center of the $Fe2p_{3/2}$ peak shifts to 710.7 ± 0.10 eV. The location of the Fe2p3/2 The binding energies, peak separation and satellite peaks (~719 eV) observed in the Fe2p region are consistent with the Raman spectra, which suggested an α-Fe_2O_3 (hematite) phase.[51-53] Addition of Au NPs to the interface (SF configurations) is verified by the XPS survey scans shown in Fig. 4c with the appearance of Au4d and Au4f peaks. Figures 4b and 4d compare high-resolution scans of the TF and SF configurations for two different thicknesses. As expected, the Au4f signature is not observed at the surface for the TF configurations, whereas the SF configurations show peaks that are approximately centered at ~84.1 and 87.8 eV for the $Au4f_{7/2}$ and $Au4f_{5/2}$ lines, respectively. (See Table S1 for exact peak locations) The peak locations, spin-orbit splitting and peak area ratio is consistent with metallic Au^0 and previous

reports for Au/Fe_2O_3 catalysts calcined above 573K.[54] The Au 4f peak positions were previously discussed for porous α-Fe_2O_3 decorated with Au NPs.[39] For example, a negative shift of the binding energy from ~84.1 to 83.9 eV was reported to be an increased interaction of the Au NPs and Fe_2O_3 support. A small negative shift in binding energy (i.e., compared to bulk gold) is observed for the thinnest SF configuration with Au NPs at the surface. However, the shift in this study is smaller. Moreover, the higher binding energy of the Fe_2O_3 $2p_{3/2}$ peak for the SF electrodes by 0.1 eV compared to the TF electrodes (i.e., after the addition of the Au NPs) is possibly due to a change in surface termination resulting from concomitant reshaping of the Au NPs. For example, it is possible the surface has a small surface termination of α-FeOOH, which has a reported binding energy peak location of ~710.2 eV.[50] In addition, DB and EM configurations were analyzed and showed the presence and absence of Au at the surface, respectively. The XPS analysis of the TF, SF, EM and DB electrodes confirms the α-Fe_2O_3 over-coating, as well as evidence that mixing of Au NPs at unintended depths after annealing is avoided. The XPS findings indicate controlled fabrication for a direct comparison of the photo-electrochemical performance. The Au NP location is important for identifying the contributions of the Au and α-Fe_2O_3, the interplay of the interface formed at the Au/α-Fe_2O_3 boundary, as well as the charge extraction dynamics of the photo-electrodes.

High-resolution scans of the O1s region are compared in Fig. 5 for the different TF and SF configurations. The TF and SF electrodes show a main peak at ~529.8 eV (O1s Peak 1) with a shoulder to the high binding energy side and peak position of ~530.9 eV (O1s Peak 2). Table S1 shows the O1s fittings with the peak locations, peak FWHM, peak area (%) and Std. Dev. (%) for O1s Peak 1 and O1s Peak 2. The low and high O1s binding energy peaks are associated with oxygen atoms in the Fe_2O_3 lattice and hydroxyl groups in the lattice, respectively.[39,44] For a

nominal 25 nm α-Fe_2O_3 thickness (i.e., TF and SF electrodes), the oxygen atoms associated with hydroxyl groups in the lattice are increased relative to the oxygen atoms in the Fe_2O_3 lattice. Moreover, thinner α-Fe_2O_3 films possess increased hydroxyl groups compared to thicker α-Fe_2O_3 films, which is evident by a decreased (O1s Peak 1):(O1s Peak 2) area ratio. For thicker α-Fe_2O_3 films, the hydroxyl groups decrease with an increased (O1s Peak 1):(O1s Peak 2) area ratio, whereby the SF and TF ratios approach similar values. Interestingly, the addition of Au NPs to the surface appears to be the main contributing factor for the increased O1s Peak 2 area especially for thinner α-Fe_2O_3 films. Since the gold concentration at the surface is the same for each SF configuration, it is determined that the ultra-thin film also contributes to the increased oxygen population at the surface. Therefore, the combination of Au NP reshaping, oxidation of Fe_xO_y → α-Fe_2O_3, and texturing of the Au back contact provide appropriate conditions to generate a more hydroxyl-group rich Au/α-Fe_2O_3 perimeter at the electrode interface.

Figure 6 shows the UV-visible Φ_{Abs} spectra for TF, SF, DB and EM configurations for two different α-Fe_2O_3 thicknesses. Figure 6a shows that the 25 nm α-Fe_2O_3 layer deposits reach a maximum Φ_{Abs} of ~90% at ~600 nm for the SF, EM and DB configurations. In contrast, the TF configuration has a lower Φ_{Abs} suggesting that the addition of Au NPs at the surface and/or within the α-Fe_2O_3 film enhances the overall Φ_{Abs}, especially at energies below the band edge (i.e., ~2 eV as determined from a Tauc plot analysis of the α-Fe_2O_3 layer and shown in Fig. 6a inset).[17, 55-56] The Tauc plot is made by plotting the $(\alpha h\nu)^2$ vs. hv to quantify the onset of absorption as previously reported.[56] As the film thickness is decreased the relative (SF25):(TF25) Φ_{Abs} ratio is also decreased. Fig. 6b compares the different configurations for α-Fe_2O_3 layer nominal thicknesses of 50 nm. The overall Φ_{Abs} in Fig. 6b is lower compared to Fig. 6a, except for the EM and DB configurations, which have a noticeable red-shift in Φ_{Abs} (~100

nm more positive) and a Φ_{Abs} close to that of their 25 nm thick counterparts observed in Fig. 6a. The red-shift in the surface plasmon resonance maximum is commonly observed for NPs encased in a media with an increased dielectric function.[34] The SF, EM and DB configurations have an increased Φ_{Abs} compared to the TF configuration. It is important to note that we compared simulations for the SF, EM and DB configurations for Au NPs with diameters of 32 nm (i.e., within the Au NP diameter average shown in Fig. S3b). In addition, we compared DDA simulations for different Au NPs sizes located at the surface (i.e, ranging from 32 to 64 nm in diameter). There are essentially two contributions to the Φ_{Abs} at $\lambda > 625$ nm. The first contribution is due to the reflective Au backing layer. The second Φ_{Abs} contribution is from Au NPs with diameters ≥ ~42 nm. However, since the TF configuration (i.e., for a comparable thickness) have a similarly increased Φ_{Abs} at longer wavelengths it is determined that the contribution at $\lambda > 625$ nm is primarily due to the underlying Au/α-Fe_2O_3/FTO substrate and not Au NPs > 32 nm in diameter at the surface. The electrode performance is evaluated to understand how the interplay between Au/α-Fe_2O_3, as well as the different Φ_{Abs} features effects the photo-electrochemical results of the small molecule (SMO) and water (WO) oxidation reactions.

The TF, SF, EM and DB configurations were photo-electrochemically compared first by monitoring the open-circuit potential (OCP) under 10 sec. interval light-chopping (AM1.5G) in the presence and absence of 0.5M EtOH in 0.1M KOH prior to performing electrocatalytic experiments. Figure S6 shows the photopotential ($\Delta OCP = OCP_{Light} - OCP_{Dark}$) with markedly different responses for the various configurations. The photo-voltage measurements probe the Fermi levels under equilibrium and quasi-equilibrium conditions as previously suggested.[40] Illuminating the thinnest TF configuration negatively shifts the OCP ~10 mV, however the shift

is short-lived (~1 sec.) and positively decays to a nearly constant value after ~5 sec. Turning off the illumination results in a nearly symmetric overshoot (i.e., relative to the maximum negative shift) in the positive charge accumulation direction, which then negatively decays to a nearly constant value after ~5 sec. The oscillating negative (positive) accumulation after the respective light (dark) irradiation suggests that the TF configuration undergoes e^--h^+ pair separation that is followed by an undesirable recombination and thermalization.[57-58] The large photopotential spike observed for the TF configuration may be due to recombination of carriers that are able to separate under illumination but unable to sustain charge separation in the absence of a bias. This is further illustrated by both the ΔOCP and the TF switching becoming less pronounced with increasing α-Fe_2O_3 thickness considering the minority carrier diffusion length reported for n-type α-Fe_2O_3.[38] The addition of Au NPs to the TF surface results in a much larger ΔOCP and a sustained photo-potential after light irradiation. Switching the light off causes a rapid decay of the current to the initial OCP baseline without the overshoot observed for the TF configuration. The trends for the maximum ΔOCP achieved are qualitatively like the TF configurations (i.e., comparing only the maximum negative charge accumulation region), however the SF electrodes possess nearly an order-of-magnitude larger ΔOCP shift for the best configuration. The rapid light on/off response of the SF configurations suggests that the time to quasi-equilibrium conditions is rapid as opposed to the other configurations. It should be noted that the ΔOCP in 0.1M KOH is larger for the SF configurations by ~30-40 mV. In contrast, the EM & DB configurations (Fig. S6c & S6d, respectively) have much smaller ΔOCPs, and are ~1 and 2 orders-of-magnitude lower than the TF and SF configurations, respectively. The difference between the TF and SF electrodes is attributed to the addition of Au NPs at the solution-electrode interface. However, simply adding Au NPs to the surface of the EM configurations (e.g., to

create the DB electrode) is not enough to enhance and recover the large ΔOCP observed for the SF electrodes.

To compliment the ΔOCP experiments, light-chopping (AM1.5G) chronoamperometry (10 sec. intervals) was performed for the EtOH oxidation reaction (EOR). Figure 7 shows three different SF configurations compared at different overpotentials (η) for the EOR illuminated with AM1.5G solar-simulated light. At a relatively low overpotential (η = 0.6V) the EOR activity is approximately equal for the different thicknesses. (Note: Here we denote η as the measured potential minus 0V vs. RHE) Incident light generates a transient increase in the current response which quickly transitions to a sustained steady-state current of approximately equal magnitude for the different α-Fe_2O_3 thicknesses. The magnitude of the transient response decreases with increasing η for all configurations. Moreover, the SF25 electrode revealed the largest steady-state current response at all η with the transient response nearly disappearing for η ≥ 1.0V. The square-wave function means charge carriers separate quickly at the overpotentials. When the η ≈ 1.0-1.1 V, the WO process is initiated yielding a mixture of the WO/SMO reactions. The decrease in the transient current and the increase in the steady-state currents are indicative of decreased recombination processes under anodic biasing.[21, 58] Furthermore, the decrease in recombination rate is evident by the disappearance of the anodic spike (i.e., light on) and slow disappearance of the cathodic spike (i.e., light off). The current density was compared for the TF, SF, EM and DB electrodes with the largest photopotential (Fig. S8). The SF electrodes show nearly an order-of-magnitude steady-state current enhancement compared to the TF, EM and DB configurations for the η = 0.8-1.0 V potential range. For the EM and DB configurations, following light irradiation, the holes are not able to efficiently separate from photogenerated electrons leading to a decay in photo-excited current. For example, it was

previously observed that embedding Au NP in hematite resulted mainly in an electrochemical increase rather than an optical increase.[59] It is interesting to note that the DB configuration exhibits the next best steady-state current albeit much lower than the SF current increase. It may be of interest to physically separate the Au NP from the semiconductor junction, thus avoiding recombination of photo-generated carriers and exciting the nearby semiconductor through a plasmon-induced resonance energy transfer process for promoting SMO reactions. .[40, 60,30]

To better understand the different configurations and decouple contributions of the Au and α-Fe_2O_3, a CWL method was developed with laser wavelengths chosen above and below the α-Fe_2O_3 band gap. Figure 8 shows slow-scan linear sweeps (2 mV s^{-1}) of the TF and SF electrodes under chopped laser irradiation (~25 sec. intervals). Figure 8 compares the current density response for λ = 532 and 785 nm wavelength excitations and the TF25/SF25 and TF50/SF50 configurations, respectively. For both TF25 and TF50 configurations shown (i.e., λ = 532 nm) the onset potential for oxidation begins at ~1.0-1.1 V, which is consistent with previous reports on pristine α-Fe_2O_3 electrodes for water oxidation.[44] Moreover, very little current density enhancement is observed for the λ = 785 nm excitation, which is expected considering the band edge of α-Fe_2O_3. Therefore, the light-trapping design for the TF configuration does not allow for photo-enhancements at below band-gap excitations, which was discussed in a recent review.[30] In contrast, the SF25 and SF50 configurations show current density enhancements at much lower η with the response for the SF25 greater than SF50 for η < 1.0V. Figures S9a-d show scans in KOH only solutions with little to no activity observed for potentials less than η ≈ 1.1V (i.e., at both λ = 532 and 785 nm excitations). It is instructive to dissect Figure 8 into potential regions that are more negative (positive) of the WO region. In the presence of alcohol molecules, the WO region (i.e., more positive than η ≈ 1.1 V) is complicated

by a mixture of the two oxidation processes from the alcohol molecule and water. Moreover, the SMO region (i.e., more negative than $\eta \approx 1.1$ V) has a considerably larger light-driven current contribution for SF configured electrodes. Interestingly, the light-driven current density increase for the $\lambda = 785$ nm excitation is only observed for SMO reactions with Au NPs at the α-Fe_2O_3 interface. The excitation energies can generate hot carriers that have energies higher than the Schottky barrier at a metal-semiconductor interface, thus directly injecting into the conduction band. The metal-semiconductor coupling (i.e., with a thin semiconductor film) has been described in terms of non-thermal energetic distribution with energetic carriers above the conduction band.[30] The above-below band-gap excitations were analyzed with-respect-to the electrochemical activity of the electrode configurations via discrete dipole approximation simulations.

Fig. 9a-b shows normalized volume-integrated near-field enhancements, $\rho(\lambda, \varphi)$, derived from Eq. 3 and the $|E/E_0|^2$ enhancements obtained using DDA simulations. A volume region of approximately twice the minority carrier diffusion length in α-Fe_2O_3 (~5 nm diffusion length of minority carriers) was used to evaluate the $\rho(\lambda,\varphi)$ as previously reported and highlighted in the inset of Fig. 9a for Region 1.[56, 61-62] The $\rho(\lambda, \varphi)$ was also investigated for Au NPs of different sizes, the entirety of the α-Fe_2O_3 layer, the solution phase, and other regions of interest, however the results did not correlate with the experimental observations. As a result, we only discuss the most pertinent interfacial enhancements derived from the $\rho(\lambda,\varphi)$. Figure 9a shows that the $\rho(\lambda,\varphi)$ increased with increasing λ until a maximum was reached followed by a decay in the $|E/E_0|^2$enhancement. For the thinnest TF electrodes, the enhancement is observed near the band-edge of α-Fe_2O_3, however with increasing thickness the enhancement shifts to longer wavelengths. Fig. 9b shows the $\rho(\lambda,\varphi)$ after the addition of the Au NPs at the solution-electrode

interface for the SF configuration. Two different regions (Regions 3 and 4) were considered for the $\rho(\lambda,\varphi)$ as shown in the inset in Fig. 9b. For a given α-Fe_2O_3 thickness, the SF configurations yield a larger $\rho(\lambda,\varphi)$ at λ = 532 and 785 nm. The $|E/E_0|^2$ enhancements are related to the AM1.5G solar-irradiated electrochemical results with the current density increase consistent with the $\rho(\lambda,\varphi)$ findings. However, the enhancement observed for the TF configurations at longer wavelengths (e.g., ~785 nm for comparison) is not observed experimentally for lower η. In contrast, for a λ = 532 nm excitation, the $\rho(\lambda,\varphi)$ does correspond in terms of WO or mixed SMO/WO reactions. Therefore, the near-field enhancement alone is not enough to describe the photo-electrochemical activity of TF configurations for the SMO region at low η. However, the SF electrodes with addition of Au NPs at the surface follows the relative $\rho(\lambda,\varphi)$ model trends. Fig. 8a-b shows that the λ = 532 nm-excited current density response for SF25 > SF50 (i.e., compared at ~1.0 V) is approximately 2× greater, which is close to a ratio of the $(\rho(\lambda,\varphi)_{SF25})$:$(\rho(\lambda,\varphi)_{SF50})$. Moreover, the λ = 785 nm-excited current density response for SF50 is only 1.3× that of SF25, which is close to the ratio of the simulated $(\rho(\lambda,\varphi)_{SF50})$:$(\rho(\lambda,\varphi)_{SF25})$. For comparison, Fig. 9c-e show near-field cross-sections of the different SF, EM and DB configurations for a given thickness, and the region of interest particularly located at the solution-electrode interface. The EM and DB structures have pronounced enhancements located within the α-Fe_2O_3 layer, however this does not extend to the solution-electrode interface, which is of considerable importance for electrocatalytic reactions. At the surface, we see a 4-5× lower $\rho(\lambda,\varphi)$ for the EM and DB at λ = 600 nm (i.e., maximum Φ_{Abs} shown in Fig. 6a) compared to the TF and SF configurations. The $\rho(\lambda,\varphi)$ model is further evaluated in terms of the IPCE (%) as shown in Fig. 10.

The IPCE (%) was determined for the TF and SF electrodes and two different α-Fe_2O_3 thicknesses. The IPCE(%) was calculated using Eq. 1 for λ = 532 and 785 nm at different potentials in the SMO and WO regions. Figures S10a-f shows $|E/E_0|^2$ cross-sections for the SF electrodes at relevant wavelengths for the CWL experiments (Fig. 10a-d). The cross-sections highlight the relevant enhancements for decoupling the above-below α-Fe_2O_3 band-gap excitations and the surface-configured Au NPs. A potential-dependent mechanism at λ = 532 and 785 nm is apparent for both the SMO and WO regions. Interestingly, the IPCE(%) for the SF25 is 2× that of the SF50 configuration in the SMO region for the EOR and the λ = 532 nm excitation. At higher η the TF configuration activities exceed that of the SF electrodes, i.e. for a comparable α-Fe_2O_3 thickness. The efficacy of the SF electrodes was also evaluated for other SMO reactions including MeOH and EG molecules (Fig. 10c). The maximum IPCE (%) achieved (SMO region) is observed for the SF25 electrodes with the current efficiency enhancements as follows: EG ≥ EtOH > MeOH > KOH Only. At low η, all small molecules have enhanced activities relative to KOH only media. The larger photo-enhanced EtOH oxidation activity compared to the MeOH oxidation activity was also observed for gold nanofiber electrodes yielding an increase of 61 and 107 %, respectively, due to photo-excitation.[19] In the WO region, EG ≥ MeOH ~ EtOH > KOH. The IPCE (%) for the KOH only media is only substantial at η ≥ 1.1V, whereby the TF and SF configurations for the thinnest configuration shows the best WO enhancement. Since the SF configurations demonstrated the largest IPCE (%) at low η for SMO this suggests that the mechanism of photo-electrochemical enhancements for SMO and WO reactions are different. A noticeable increase in the IPCE (%) of the SMO reactions is observed at λ = 785 nm for the SF electrodes compared to the TF

configurations with an onset potential $\eta \approx 0.6$ V and activities of EG > EtOH > MeOH > KOH only media.

Figure 11 shows band energy diagrams for the different processes considered in this study. Figure 11a shows the density of states (DOS) of α-Fe_2O_3. The α-Fe_2O_3 has a band-gap of ~1.9-2.2 eV as previously reported and consistent with the DOS calculations shown.[38] The redox potential difference for H_2O/H_2 to H_2O/O_2 is a total 1.23V vs. RHE. The SMO/CO_2 redox potential is situated positive of the H_2O/H_2 position, which is commonly observed in fuel cell catalysis and plasmonic catalysis on gold nanofiber electrodes.[10,19] Figure 11b shows the band energy diagram for a typical TF photoelectrode. At $\eta < 1.0$ V, there is little to no photocurrent increase observed for above or below band-gap excitations. At $\eta > 1.0$ V, only above band gap excitations ($h\nu > E_g$) is there a substantial photo-current observed for the TF electrodes. A previous study showed that resonantly trapped light in quarter-wave thin α-Fe_2O_3 films layered on back metal reflectors amplified the intensity close to the water interface allowing photo-generated holes to oxidize water before bulk recombination.[25, 64] However, the resonantly-trapped light is only suitable at higher η and above band-gap energies. Moreover, it was previously shown that a substantial positive bias enhances the h^+ lifetime by overcoming charge recombination processes.[65] For example, transient absorption spectroscopy (TAS) on Si-doped α-Fe_2O_3 electrodes determined that an anodic bias decreased the 50% decay time of e^--h^+ recombination by ~33× for the WO reaction.[57] In contrast, SF electrodes with Au NPs situated at the hematite interface exhibit photo-enhancements for low and high η. Additionally, the photo-enhancements are observed for $h\nu > E_g$ and $h\nu < E_g$ excitations. Figure 11e shows that there are two possible mechanisms for excitation. For $h\nu > E_g$, the process may occur by directly exciting the α-Fe_2O_3 layer, as well as interband transitions in the Au NPs. Additionally, for $h\nu < E_g$, the

α-Fe_2O_3 layer is not directly excited and intraband transitions in the Au NP are excited resulting in direct electron transfer (DET) process into the conduction band of α-Fe_2O_3. The hot electrons generated from direct injection and near-field coupling are able to pass into the conduction band of α-Fe_2O_3 when energy levels are greater than the Schottky barrier (φ_b).[63] Figure 11d shows the DOS of Au with the sp-band and d-band contributions with approximate locations near the fermi level for exciting intra- and inter-band excitations. The different processes for above-below band-gap excitations have been discussed elsewhere.[30] Our findings along with previous observations highlight the difference in the SMO and WO region reactions with emphasis placed on the Au/α-Fe_2O_3 interface. In general, location of Au NPs at the surface couples light into the ultra-thin α-Fe_2O_3 layer, which in combination with the resonantly-trapped light enhances the Φ_{Abs} of the electrode and extends the lifetime of minority carriers and/or the number of carriers generated for reaction participation. When the Au NPs are located within the EM or DB configurations the $|E/E_0|^2$ is coupled to the α-Fe_2O_3 yielding increased Φ_{Abs} locally however the additional Au/α-Fe_2O_3 interfaces within the semiconductor may also serve as electron-hole trap centers, thus impeding efficient carrier collection evidenced by the decreased IPCE (%) for a comparable α-Fe_2O_3 thickness. The collection efficiency of the EM and DB might be enhanced with even thinner α-Fe_2O_3 layers (i.e., less than the thicknesses considered), however the electron-beam evaporation method undertaken in this study may not be sufficient. In addition, the existence of a reflective Au back contact layer has been shown to support surface plasmon polariton modes[31, 66], however due to the distance away from the solution-electrode interface these modes do not appear to play an important role in the experimentally determined SMO electrochemical activity at low η (Region 1 inset in Fig. 9a). Moreover, the ρ(λ,φ) was also determined for each configuration for Region 2 (Inset Fig. 9a), and since the results are similar

this is ruled out as a significant contributing factor at low η. The diameter of the metal NP has been discussed in terms of hot carrier production probability with NPs believed to produce a large fraction of hot carriers under light excitation.[22] In this regard, Fig. S3b shows that there is a distribution of Au NPs at the surface that range from ~10-50 nm in diameter. However, a recent experimental study found that a rather large distribution of NP diameters resulted in similar carrier lifetime measurements, whereby the light excitation was more efficient in generating additional hot carriers when targeting the interband transitions in the metal.[67] Finally, the increased oxygenated surface species at the Au/α-Fe_2O_3 surface and their interactions with alcohol molecules may play an important role. For example, the metal/metal-oxide interface plays an important part in the Mars-van Krevelen mechanism, where the presence of Au has been shown to facilitate the formation of oxygen vacancies at the α-Fe_2O_3 boundary.[68] In the present study, increased oxygenated species at Au/α-Fe_2O_3 surface was observed and correlated with an increased O1s peak contribution at higher binding energies. (We denote this as "P" in Figure 11e-f) The formation of these oxygenated species is in part due to a strong metal oxide support-metal interaction also shown to be useful for oxidation reactions.[69] The shift in Au 4f binding energy is consistent with a strong support metal interaction, however the relative shift was slightly lower than that previously reported.[39] Furthermore, the $Fe2p_{3/2}$ peak positions for the SF electrodes indicated that there may the presence of α-FeOOH at the surface suggesting an additional source of the oxygenated species. The source of the the hydroxyl species originates only from the addition of the Au NPs at the α-Fe_2O_3 followed by annealing. Therefore, the fabrication method presented yields not only a distribution of Au NPs at the photo-electrochemical interface for hot electron generation, but also establishes a method to create more hydroxyl-rich Au/α-Fe_2O_3 perimeter/interface. However, the perimeter oxygen-rich

(hydroxyl groups) must be available for reactant molecule attachment to undergo successful oxidation. This is the case for the surface-configured electrodes. In contrast, the embedded and thin film configurations do not populate the electrochemical interface with these groups, which may be an additional source of low activity due to trap centers. In summary, the theoretical and experimental findings identify optimal metal-semiconductor couplings that increase the photo-oxidation behavior of SMO and WO reactions. An emphasis is placed on strategies to obtain enhanced activities at low temperatures and η with particular attention to the photo-electrochemical interface and corresponding electromagnetic ρ(λ,φ) simulations.

CONCLUSIONS

Photo-electrodes comprised of Au NPs and α-Fe_2O_3 were designed in different configurations to understand how the metal-semiconductor coupling played not only a role in the WO reaction, but also participated in different SMO reactions including EtOH, MeOH and EG oxidation. A fabrication process was established via multiple electron beam evaporation and annealing steps to generate Au/α-Fe_2O_3 electrodes with Au NPs of ~30 ± 8 nm in diameter within and/or at the surface of the photo-electrodes. TEM, HAADF-STEM and EDS mapping confirm the thin electrode structures with the Au reflective contact layer, as well as a continuous α-Fe_2O_3 film with Au NPs. The best Au/α-Fe_2O_3 coupling resulted in a substantial SMO current density increase for SMO reactions under AM1.5G solar-simulated light excitation compared to baseline configurations at low η. In contrast, the addition of Au NPs provided less of a relative photo-enhancement at large η where competing SMO and WO reactions occur. At low η, the SMO IPCE (%, λ = 532 nm) for the SF25 electrode increased as follows: EG ≥ EtOH > MeOH >

KOH only media. At light excitation energies below the band-gap a current density increase was also observed, but only for the surface-configured films with Au NPs positioned at the interface. The IPCE (%, λ = 785 nm) at low η for the SF25 electrode was as follows EG > EtOH > MeOH > KOH only media. The current density increase correlated with electromagnetic simulations and $\rho(\lambda,\varphi)$ determined over select regions of the Au/α-Fe_2O_3 catalytic electrochemical interface. The regions evaluated included the Au NP, the α-Fe_2O_3 layer, the reflective Au back contact, and various Au/α-Fe_2O_3 combinations. The ultra-thin α-Fe_2O_3 film supported on the reflective Au back contact is believed to resonantly trap the incident light enhancing the WO or a mixture of SMO/WO (i.e., in the presence of alcohol molecules) reactions at η > 1.1 V. The addition of Au NPs to the α-Fe_2O_3 thin film further enhanced the IPCE (%) by lowering the η required to drive different SMO reactions by nearly 400 mV with a unique signature current density increase for λ = 785 nm excitations below the α-Fe_2O_3 band edge. In addition, the fabrication process yielded a hydroxyl-terminated Au/α-Fe_2O_3 interface especially for increasingly thin α-Fe_2O_3 films as determined by XPS. It is believed that the increase in oxygenated species at the surfaces plays a unique role in the photo-electrochemical activity providing potential adsorption sites for catalytic oxidation. The physical characterizations and photo-electrochemical analysis provides a foundation for future studies that seek to understand and enhance light-induced SMO reactions. Furthermore, the electromagnetic simulations highlight the importance of the $\rho(\lambda,\varphi)$ determined at the electrode-solution interface providing a design criteria for photo-electrocatalytic SMO reactions.

ACKNOWLEDGEMENTS

The authors gratefully acknowledge the U.S. Department of the Army and U.S. Army Material Command (AMC) for supporting this work. The authors would like to thank Drs. Wen-An Chiou, Sz-Chian Liou and Jiancun Rao at the Maryland Nanocenter for assistance with FIB-SEM sample preparation and HAADF-STEM imaging. The authors would also like to acknowledge Dr. Cynthia Lundgren for helpful discussions. The authors additionally acknowledge Drs. Jiangtian Li, Jonathan Boltersdorf and Collin R. Becker for helpful discussions, as well as Dr. Li Sun at Pine Instruments for cooperative discussions leading to the development of a custom-built Teflon cell for AM1.5 solar-simulated experiments. Finally, the authors would like to thank the photo-electrochemistry team for continued support and discussions.

REFERENCES

1. Geraldes, A. N.; da Silva, D. F.; Pino, E. S.; da Silva, J. C. M.; de Souza, R. F. B.; Hammer, P.; Spinacé, E. V.; Neto, A. O.; Linardi, M.; dos Santos, M. C., Ethanol electro-oxidation in an alkaline medium using Pd/C, Au/C and PdAu/C electrocatalysts prepared by electron beam irradiation. *Electrochimica Acta* **2013,** *111* (Supplement C), 455-465.
2. Grew, K. N.; McClure, J. P.; Chu, D.; Kohl, P. A.; Ahlfield, J. M., Understanding Transport at the Acid-Alkaline Interface of Bipolar Membranes. *Journal of The Electrochemical Society* **2016,** *163* (14), F1572-F1587.
3. Qi, Z.; Geng, H.; Wang, X.; Zhao, C.; Ji, H.; Zhang, C.; Xu, J.; Zhang, Z., Novel nanocrystalline PdNi alloy catalyst for methanol and ethanol electro-oxidation in alkaline media. *Journal of Power Sources* **2011,** *196* (14), 5823-5828.
4. He, Q.; Chen, W.; Mukerjee, S.; Chen, S.; Laufek, F., Carbon-supported PdM (M=Au and Sn) nanocatalysts for the electrooxidation of ethanol in high pH media. *Journal of Power Sources* **2009,** *187* (2), 298-304.
5. Jiang, R.; Tran, D. T.; McClure, J. P.; Chu, D., A Class of (Pd–Ni–P) Electrocatalysts for the Ethanol Oxidation Reaction in Alkaline Media. *ACS Catalysis* **2014,** *4* (8), 2577-2586.
6. Wen, C.; Wei, Y.; Tang, D.; Sa, B.; Zhang, T.; Chen, C., Improving the electrocatalytic properties of Pd-based catalyst for direct alcohol fuel cells: effect of solid solution. *Scientific Reports* **2017,** *7* (1), 4907.
7. Xu, C.; Shen, P. k.; Liu, Y., Ethanol electrooxidation on Pt/C and Pd/C catalysts promoted with oxide. *Journal of Power Sources* **2007,** *164* (2), 527-531.

8. Huang, S.-Y.; Ganesan, P.; Park, S.; Popov, B. N., Development of a Titanium Dioxide-Supported Platinum Catalyst with Ultrahigh Stability for Polymer Electrolyte Membrane Fuel Cell Applications. *Journal of the American Chemical Society* **2009,** *131* (39), 13898-13899.
9. Li, Y.; Liu, C.; Liu, Y.; Feng, B.; Li, L.; Pan, H.; Kellogg, W.; Higgins, D.; Wu, G., Sn-doped TiO2 modified carbon to support Pt anode catalysts for direct methanol fuel cells. *Journal of Power Sources* **2015,** *286*, 354-361.
10. Liu, Y.; Liu, C.; Yu, X.; Osgood, H.; Wu, G., CeO2-modified alpha-MoO3 nanorods as a synergistic support for Pt nanoparticles with enhanced COads tolerance during methanol oxidation. *Phys Chem Chem Phys* **2016,** *19* (1), 330-339.
11. Lu, C.-L.; Prasad, K. S.; Wu, H.-L.; Ho, J.-a. A.; Huang, M. H., Au Nanocube-Directed Fabrication of Au−Pd Core−Shell Nanocrystals with Tetrahexahedral, Concave Octahedral, and Octahedral Structures and Their Electrocatalytic Activity. *Journal of the American Chemical Society* **2010,** *132* (41), 14546-14553.
12. DeRita, L.; Dai, S.; Lopez-Zepeda, K.; Pham, N.; Graham, G. W.; Pan, X.; Christopher, P., Catalyst Architecture for Stable Single Atom Dispersion Enables Site-Specific Spectroscopic and Reactivity Measurements of CO Adsorbed to Pt Atoms, Oxidized Pt Clusters, and Metallic Pt Clusters on TiO2. *Journal of the American Chemical Society* **2017,** *139* (40), 14150-14165.
13. Strasser, P.; Koh, S.; Anniyev, T.; Greeley, J.; More, K.; Yu, C.; Liu, Z.; Kaya, S.; Nordlund, D.; Ogasawara, H.; Toney, M. F.; Nilsson, A., Lattice-strain control of the activity in dealloyed core–shell fuel cell catalysts. *Nature Chemistry* **2010,** *2*, 454.
14. Beden, B.; Çetin, I.; Kahyaoglu, A.; Takky, D.; Lamy, C., Electrocatalytic oxidation of saturated oxygenated compounds on gold electrodes. *Journal of Catalysis* **1987,** *104* (1), 37-46.
15. Zhang, J.-h.; Liang, Y.-j.; Li, N.; Li, Z.-y.; Xu, C.-w.; Jiang, S. P., A remarkable activity of glycerol electrooxidation on gold in alkaline medium. *Electrochimica Acta* **2012,** *59* (Supplement C), 156-159.
16. Moskovits, M., The case for plasmon-derived hot carrier devices. *Nat Nanotechnol* **2015,** *10* (1), 6-8.
17. Li, Y.; Wei, X.; Zhu, B.; Wang, H.; Tang, Y.; Sum, T. C.; Chen, X., Hierarchically branched Fe2O3@TiO2 nanorod arrays for photoelectrochemical water splitting: facile synthesis and enhanced photoelectrochemical performance. *Nanoscale* **2016,** *8* (21), 11284-11290.
18. Qi, D.; Zheng, L.; Cao, X.; Jiang, Y.; Xu, H.; Zhang, Y.; Yang, B.; Sun, Y.; Hng, H. H.; Lu, N.; Chi, L.; Chen, X., Bio-inspired antireflective hetero-nanojunctions with enhanced photoactivity. *Nanoscale* **2013,** *5* (24), 12383-12387.
19. Chen, D.; Zhang, R.; Wang, R.; Negro, L. D.; Minteer, S. D., Gold Nanofiber-Based Electrodes for Plasmon-Enhanced Electrocatalysis. *Journal of The Electrochemical Society* **2016,** *163* (14), H1132-H1135.
20. Cushing, S. K.; Li, J.; Meng, F.; Senty, T. R.; Suri, S.; Zhi, M.; Li, M.; Bristow, A. D.; Wu, N., Photocatalytic activity enhanced by plasmonic resonant energy transfer from metal to semiconductor. *J Am Chem Soc* **2012,** *134* (36), 15033-41.
21. McClure, J. P.; Grew, K. N.; Das, N. C.; Chu, D.; Baker, D.; Strnad, N.; Gobrogge, E., Plasmonic-Enhancement of the Electro-Oxidation of Ethanol in Alkaline Media with Au-Fe2O3 Thin Film, Embedded, Sandwich and Surface Configurations. *MRS Advances* **2017,** *2* (55), 3397-3402.
22. Narang, P.; Sundararaman, R.; Atwater, H. A., Plasmonic hot carrier dynamics in solid-state and chemical systems for energy conversion. *Nanophotonics* **2016,** *5* (1).

23. Warren, S. C.; Thimsen, E., Plasmonic solar water splitting. *Energy & Environmental Science* **2012,** *5* (1), 5133-5146.
24. Lee, J.; Mubeen, S.; Ji, X.; Stucky, G. D.; Moskovits, M., Plasmonic Photoanodes for Solar Water Splitting with Visible Light. *Nano Letters* **2012,** *12* (9), 5014-5019.
25. Dotan, H.; Kfir, O.; Sharlin, E.; Blank, O.; Gross, M.; Dumchin, I.; Ankonina, G.; Rothschild, A., Resonant light trapping in ultrathin films for water splitting. *Nature Materials* **2012,** *12*, 158.
26. Hou, W.; Hung, W. H.; Pavaskar, P.; Goeppert, A.; Aykol, M.; Cronin, S. B., Photocatalytic Conversion of CO2 to Hydrocarbon Fuels via Plasmon-Enhanced Absorption and Metallic Interband Transitions. *ACS Catalysis* **2011,** *1* (8), 929-936.
27. Mukherjee, S.; Libisch, F.; Large, N.; Neumann, O.; Brown, L. V.; Cheng, J.; Lassiter, J. B.; Carter, E. A.; Nordlander, P.; Halas, N. J., Hot electrons do the impossible: plasmon-induced dissociation of H2 on Au. *Nano Lett* **2013,** *13* (1), 240-7.
28. Zheng, Z.; Tachikawa, T.; Majima, T., Plasmon-Enhanced Formic Acid Dehydrogenation Using Anisotropic Pd–Au Nanorods Studied at the Single-Particle Level. *Journal of the American Chemical Society* **2015,** *137* (2), 948-957.
29. Reichert, R.; Jusys, Z.; Behm, R. J., A novel photoelectrochemical flow cell with online mass spectrometric detection: oxidation of formic acid on a nanocrystalline TiO2 electrode. *Physical Chemistry Chemical Physics* **2014,** *16* (45), 25076-25080.
30. Wu, N., Plasmonic metal-semiconductor photocatalysts and photoelectrochemical cells: a review. *Nanoscale* **2018,** *10* (6), 2679-2696.
31. Atwater, H. A.; Polman, A., Plasmonics for improved photovoltaic devices. *Nature Materials* **2010,** *9*, 205.
32. Brongersma, M. L.; Halas, N. J.; Nordlander, P., Plasmon-induced hot carrier science and technology. *Nature Nanotechnology* **2015,** *10*, 25.
33. Ng, C.; Cadusch, J. J.; Dligatch, S.; Roberts, A.; Davis, T. J.; Mulvaney, P.; Gomez, D. E., Hot Carrier Extraction with Plasmonic Broadband Absorbers. *ACS Nano* **2016,** *10* (4), 4704-11.
34. Garcia, M. A., Surface plasmons in metallic nanoparticles: fundamentals and applications. *Journal of Physics D: Applied Physics* **2011,** *44* (28), 283001.
35. Gong, J.; Mullins, C. B., Surface Science Investigations of Oxidative Chemistry on Gold. *Accounts of Chemical Research* **2009,** *42* (8), 1063-1073.
36. Kwon, Y.; Lai, S. C. S.; Rodriguez, P.; Koper, M. T. M., Electrocatalytic Oxidation of Alcohols on Gold in Alkaline Media: Base or Gold Catalysis? *Journal of the American Chemical Society* **2011,** *133* (18), 6914-6917.
37. Hebié, S.; Napporn, T. W.; Morais, C.; Kokoh, K. B., Size-Dependent Electrocatalytic Activity of Free Gold Nanoparticles for the Glucose Oxidation Reaction. *ChemPhysChem* **2016,** *17* (10), 1454-1462.
38. Sivula, K.; Le Formal, F.; Grätzel, M., Solar Water Splitting: Progress Using Hematite (α-Fe2O3) Photoelectrodes. *ChemSusChem* **2011,** *4* (4), 432-449.
39. Liu, X.; Zhang, J.; Guo, X.; Wu, S.; Wang, S., Porous alpha-Fe2O3 decorated by Au nanoparticles and their enhanced sensor performance. *Nanotechnology* **2010,** *21* (9), 095501.
40. Xu, Z.; Fan, Z.; Shi, Z.; Li, M.; Feng, J.; Pei, L.; Zhou, C.; Zhou, J.; Yang, L.; Li, W.; Xu, G.; Yan, S.; Zou, Z., Interface Manipulation to Improve Plasmon□Coupled Photoelectrochemical Water Splitting on α□Fe2O3 Photoanodes. *ChemSusChem* **2018,** *11* (1), 237-244.

41. Draine, B. T.; Flatau, P. J., Discrete-dipole approximation for periodic targets: theory and tests. *J. Opt. Soc. Am. A* **2008,** *25* (11), 2693-2703.
42. Draine, B. T.; Flatau, P. J., Discrete-Dipole Approximation For Scattering Calculations. *J. Opt. Soc. Am. A* **1994,** *11* (4), 1491-1499.
43. Flatau, P. J.; Draine, B. T., Fast near field calculations in the discrete dipole approximation for regular rectilinear grids. *Opt. Express* **2012,** *20* (2), 1247-1252.
44. Shinde, P. S.; Choi, S. H.; Kim, Y.; Ryu, J.; Jang, J. S., Onset potential behavior in [small alpha]-Fe2O3 photoanodes: the influence of surface and diffusion Sn doping on the surface states. *Physical Chemistry Chemical Physics* **2016,** *18* (4), 2495-2509.
45. Doron-Mor, I.; Barkay, Z.; Filip-Granit, N.; Vaskevisch, A.; Rubinstein, I., Ultrathin gold island films on silanized glass. Morphology and optical properties. *Chem Mater* **2004,** *16*.
46. Schaub, A.; Slepička, P.; Kašpárková, I.; Malinský, P.; Macková, A.; Švorčík, V., Gold nanolayer and nanocluster coatings induced by heat treatment and evaporation technique. *Nanoscale Research Letters* **2013,** *8* (1), 249.
47. Massey, M. J.; Baier, U.; Merlin, R.; Weber, W. H., Effects of pressure and isotopic substitution on the Raman spectrum of \ensuremath{\alpha}-${\mathrm{Fe}}_{2}$${\mathrm{O}}_{3}$: Identification of two-magnon scattering. *Physical Review B* **1990,** *41* (11), 7822-7827.
48. Rodriguez, R. D.; Sheremet, E.; Deckert-Gaudig, T.; Chaneac, C.; Hietschold, M.; Deckert, V.; Zahn, D. R. T., Surface- and tip-enhanced Raman spectroscopy reveals spin-waves in iron oxide nanoparticles. *Nanoscale* **2015,** *7* (21), 9545-9551.
49. Švorčík, V.; Kvítek, O.; Lyutakov, O.; Siegel, J.; Kolská, Z., Annealing of sputtered gold nano-structures. *Appl Phys A* **2011,** *102*.
50. Moulder, J. F.; Chastain, J., *Handbook of X-ray Photoelectron Spectroscopy: A Reference Book of Standard Spectra for Identification and Interpretation of XPS Data*. Physical Electronics Division, Perkin-Elmer Corporation: 1992.
51. Aivazoglou, E.; Metaxa, E.; Hristoforou, E., Microwave-assisted synthesis of iron oxide nanoparticles in biocompatible organic environment. *AIP Advances* **2018,** *8* (4), 048201.
52. de Faria, D. L. A.; Venâncio Silva, S.; de Oliveira, M. T., Raman microspectroscopy of some iron oxides and oxyhydroxides. *Journal of Raman Spectroscopy* **1997,** *28* (11), 873-878.
53. Tarakeshwar, P.; Finkelstein-Shapiro, D.; Hurst, S. J.; Rajh, T.; Mujica, V., Surface-Enhanced Raman Scattering on Semiconducting Oxide Nanoparticles: Oxide Nature, Size, Solvent, and pH Effects. *The Journal of Physical Chemistry C* **2011,** *115* (18), 8994-9004.
54. Park, E. D.; Lee, J. S., Effects of Pretreatment Conditions on CO Oxidation over Supported Au Catalysts. *Journal of Catalysis* **1999,** *186* (1), 1-11.
55. Shinde, S. S.; Bansode, R. A.; Bhosale, C. H.; Rajpure, K. Y., Physical properties of hematite α-Fe 2 O 3 thin films: application to photoelectrochemical solar cells. *Journal of Semiconductors* **2011,** *32* (1), 013001.
56. Sorenson, S.; Driscoll, E.; Haghighat, S.; Dawlaty, J. M., Ultrafast Carrier Dynamics in Hematite Films: The Role of Photoexcited Electrons in the Transient Optical Response. *The Journal of Physical Chemistry C* **2014,** *118* (41), 23621-23626.
57. Pendlebury, S. R.; Wang, X.; Le Formal, F.; Cornuz, M.; Kafizas, A.; Tilley, S. D.; Grätzel, M.; Durrant, J. R., Ultrafast Charge Carrier Recombination and Trapping in Hematite Photoanodes under Applied Bias. *Journal of the American Chemical Society* **2014,** *136* (28), 9854-9857.

58. Chen, H.; Liu, G.; Wang, L., Switched photocurrent direction in Au/TiO2 bilayer thin films. *Scientific Reports* **2015,** *5*, 10852.
59. Gross Koren, M.; Dotan, H.; Rothschild, A., Nano Gold Rush: On the Origin of the Photocurrent Enhancement in Hematite Photoanodes Decorated with Gold Nanoparticles. *The Journal of Physical Chemistry C* **2016,** *120* (28), 15042-15051.
60. Li, J.; McClure, J. P.; Fu, R.; Jiang, R.; Chu, D., Understanding charge transfer dynamics in QDs-TiO2 nanorod array photoanodes for solar fuel generation. *Applied Surface Science* **2018,** *429*, 48-54.
61. Liao, P.; Carter, E. A., Hole transport in pure and doped hematite. *Journal of Applied Physics* **2012,** *112* (1), 013701.
62. Zhang, X.; Li, H.; Wang, S.; Fan, F.-R. F.; Bard, A. J., Improvement of Hematite as Photocatalyst by Doping with Tantalum. *The Journal of Physical Chemistry C* **2014,** *118* (30), 16842-16850.
63. Sundararaman, R.; Narang, P.; Jermyn, A. S.; Goddard, W. A., 3rd; Atwater, H. A., Theoretical predictions for hot-carrier generation from surface plasmon decay. *Nat Commun* **2014,** *5*, 5788.
64. Dotan, H.; Sivula, K.; Gratzel, M.; Rothschild, A.; Warren, S. C., Probing the photoelectrochemical properties of hematite ([small alpha]-Fe2O3) electrodes using hydrogen peroxide as a hole scavenger. *Energy & Environmental Science* **2011,** *4* (3), 958-964.
65. Vura-Weis, J.; Jiang, C.-M.; Liu, C.; Gao, H.; Lucas, J. M.; de Groot, F. M. F.; Yang, P.; Alivisatos, A. P.; Leone, S. R., Femtosecond M2,3-Edge Spectroscopy of Transition-Metal Oxides: Photoinduced Oxidation State Change in α-Fe2O3. *The Journal of Physical Chemistry Letters* **2013,** *4* (21), 3667-3671.
66. Ahn, W.; Ratchford, D. C.; Pehrsson, P. E.; Simpkins, B. S., Surface plasmon polariton-induced hot carrier generation for photocatalysis. *Nanoscale* **2017,** *9* (9), 3010-3022.
67. Minutella, E.; Schulz, F.; Lange, H., Excitation-Dependence of Plasmon-Induced Hot Electrons in Gold Nanoparticles. *J Phys Chem Lett* **2017,** *8* (19), 4925-4929.
68. Hoh, S. W.; Thomas, L.; Jones, G.; Willock, D. J., A density functional study of oxygen vacancy formation on α-Fe2O3(0001) surface and the effect of supported Au nanoparticles. *Research on Chemical Intermediates* **2015,** *41* (12), 9587-9601.
69. Ruiz Puigdollers, A.; Schlexer, P.; Tosoni, S.; Pacchioni, G., Increasing Oxide Reducibility: The Role of Metal/Oxide Interfaces in the Formation of Oxygen Vacancies. *ACS Catalysis* **2017,** *7* (10), 6493-6513.

Figure Captions

Figure 1. Schematic of the fabrication process for creating the Au/α-Fe_2O_3 photo-electrodes. Electron-beam (EB) evaporation deposited Fe_xO_y layers onto the thicker Au-coated FTO reflective substrate (Au layer 1). Annealing (ΔT) the photo-electrode converted the Fe_xO_y layer to the α-Fe_2O_3 (hematite) film. A 5 nm Au film (Au Layer 2) was converted to Au nanoparticles (NP) after the ΔT treatment. A single ΔT is required to create the thin film (TF) and surface-film (SF) configurations, whereas two ΔT steps are required to create the embedded (EM) and distributed (DB) configurations.

Figure 2. Scanning electron microscope (SEM) images of a) thin film (TF) b) surface (SF) c) embedded (EM) and d) distributed (DB) configurations. Note: a-b are shown for 0° stage tilt, whereas c-d are shown at 15° stage tilt to highlight the over-coated Au NPs in the EM and DB configurations, as well as the surface roughness created during the annealing treatments.

Figure 3. Cross-section a) TEM image of the EM50 sample. The EM50 sample is made by first depositing a nominal 25 nm of α-Fe_2O_3 layer on the Au Layer 1 (nominal 50 nm thickness). Next, Au NPs are deposited atop the 25 nm α-Fe_2O_3 layer. Finally, 25 nm α-Fe_2O_3 layer is deposited over the Au NPs. b) HAADF-STEM image showing the FTO, Au, α-Fe_2O_3 and Au NP surface with a protective carbon coating at the surface. c) EDS mapping of the cross-section highlighting the FTO substrate, Au Layer 1, and Au NP/α-Fe_2O_3 surface. d) SEM-EDS spectra of a typical Au/ α-Fe_2O_3 photo-electrode.

Figure 4. X-ray photoelectron spectroscopy (XPS) survey scans of the different a) thin film (TF) and c) surface (SF) configurations for 25, 50 and 75 nm thick α-Fe_2O_3 layers. Corresponding XPS high-resolution spectra of the Au4f binding energy region that compares the b) SF25 and TF25 (25 nm α-Fe_2O_3 thickness) electrode and b) SF50 and TF50 (50 nm α-Fe_2O_3 thickness).

Figure 5. High-resolution XPS spectra of the O1s binding energy region that compares different α-Fe_2O_3 layer thicknesses for both the thin film (TF) and surface (SF) configurations. O1s Peak 1 refers to oxygen atoms in Fe_2O_3 lattice. O1s Peak 2 refers to hydroxyl atoms in lattice and increases with addition of Au NPs to surface and decreasing α-Fe_2O_3 film thickness. Note: 25, 50 and 75 nm α-Fe_2O_3 deposit thicknesses shown.

Figure 6. UV-visible Φ_{Abs} (%) spectra for the a) TF, SF, EM and SF with a 25 nm α-Fe_2O_3 thickness compared to b) TF, SF, EM and SF with a 50 nm α-Fe_2O_3 thickness. Note: Solid lines for TF, short dot lines for EM, dashed lines for SF, and dash-dot lines for DB. The inset in 5a shows the Tauc plot of a typical α-Fe_2O_3 used to determine the band edge and band gap energies.

Figure 7. a) Light-chopping (10 sec. intervals) for solar-simulated (AM1.5G) chronoamperometry experiments performed for three different SF configurations and three different overpotentials (η) of a) 0.6 b) 0.8 and c) 1.0V vs. RHE. Experiments performed at room temperature in 0.5M EtOH and 0.1M KOH. (Note: SF25, SF50, SF75 refers to a 25, 50 and 75-nm thick films of α-Fe_2O_3, respectively)

Figure 8. Light-chopping (25 sec. intervals) linear-sweep voltammetry (LSV) under continuous-wave laser (CWL) excitation at λ = 532 and 785 nm for a) SF25 b) SF50 c) TF25 and d) TF50. (Note: 25 and 50 nm α-Fe_2O_3 thicknesses, respectively) LSV experiments performed at room temperature in 0.5M EtOH and 0.1M KOH with a 2 mV s^{-1} scan rate.

Figure 9. Normalized volume-integrated near-field enhancements, $\rho(\lambda, \varphi)$, for a) thin film (TF) configurations with the α-Fe_2O_3 layer thicknesses ranging 10-80 nm and b) surface (SF) configurations with α-Fe_2O_3 thickness ranging 10-80 nm and Au NP diameters of 32 nm. Near-field cross-sections shown for the c) SF d) EM and e) DB configurations at the peak Φ_{Abs} shown in Fig. 5. Inset in a) show cross-sections of the TF electrode where Region 1 refers to the α-Fe_2O_3, and Region 2 refers to the interface of the Au back contact and bottom-side of the α-Fe_2O_3 layer. Inset in b) shows a cross-section of the SF electrode where Region 3 refers to the Au NP surface, and Region 4 refers to the α-Fe_2O_3 at the solution-electrode interface.

Figure 10. Incident-photon-to-current efficiencies, IPCE (%), for the TF and SF electrodes with 25 and 50 nm α-Fe_2O_3 thicknesses. IPCE (%) determined from laser irradiated experiments for the ethanol (EtOH) oxidation reaction and TF25, TF50, SF25 and SF50 electrodes at a) λ = 532 nm and b) λ = 785 nm wavelength excitations. IPCE (%) comparison of different small molecule (SMO) and water oxidation (WO) reactions for methanol (MeOH), ethylene glycol (EG) and KOH only media and the SF25 photo-electrode at c) λ = 532 and d) λ = 785 nm wavelength excitations. The dashed line indicates the transition from the SMO at low η to either the WO only or mixed SMO/WO region at high η. Note: Error bars shown for approximately every 5th measurement for clarity.

Figure 11. Band energy diagrams for the TF (Fig. 11a-c) and SF (Fig. 11d-f) samples. The density of states (DOS) for (Fig. 11a) α-Fe_2O_3 and (Fig. 11d) Au are shown on the left axis. The redox potentials for the SMO and WO regions are also shown (Fig. 11a). The band energy diagrams are shown for the low η (Fig. b and e) diagrams, as well as the high η region. Direct electron transfer (Direct) from the photo-excited Au NP injects energetic electrons (E_{e^-}) into the conduction band of the α-Fe_2O_3 is shown for $h\nu > E_g$, whereas near-field enhancements (Near-field) are observed at $h\nu > E_g$. The SF samples also have an increased O1s peak 2 as determined by XPS, which we denote as (P). Note: Green arrows (left axis) denote $h\nu > E_g$, whereas the red arrows (left axis) denote $h\nu < E_g$.

Figures

Figure 1

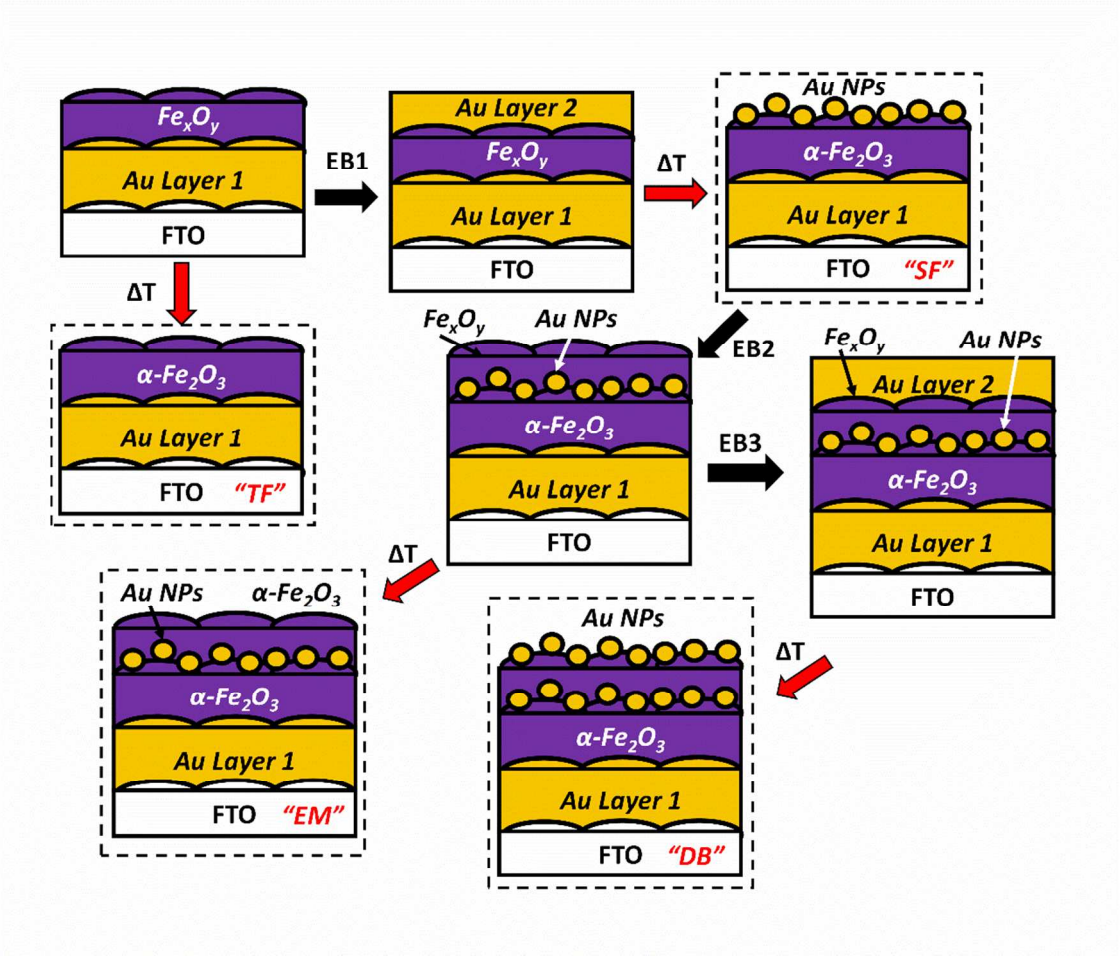

Figure 2

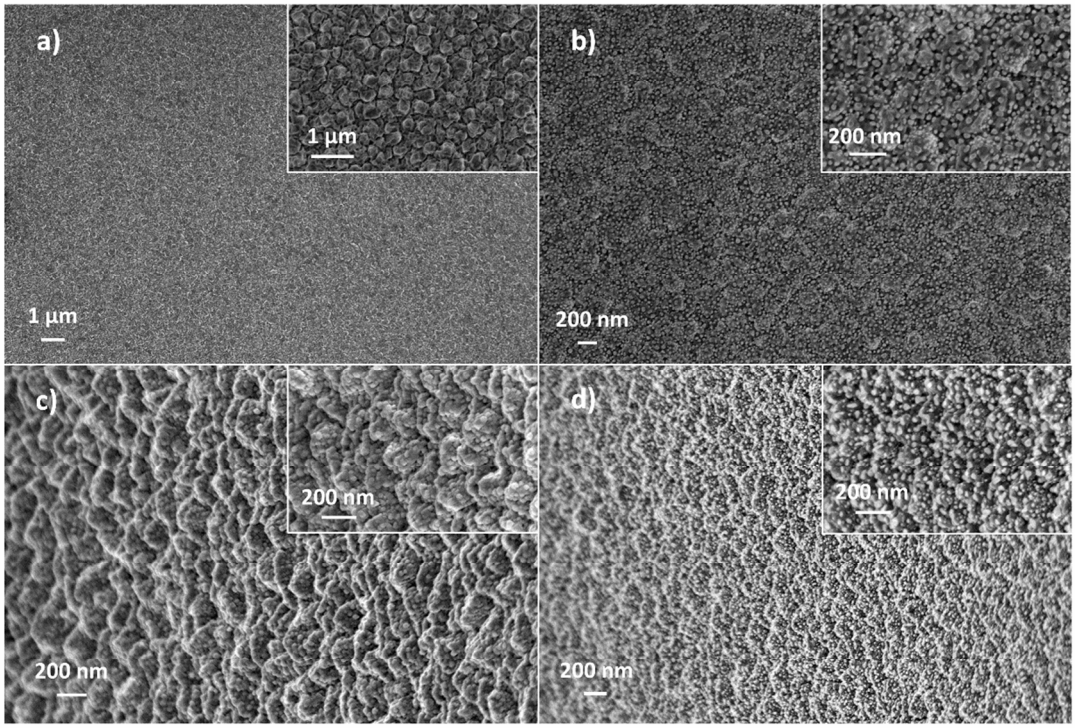

Figure 3

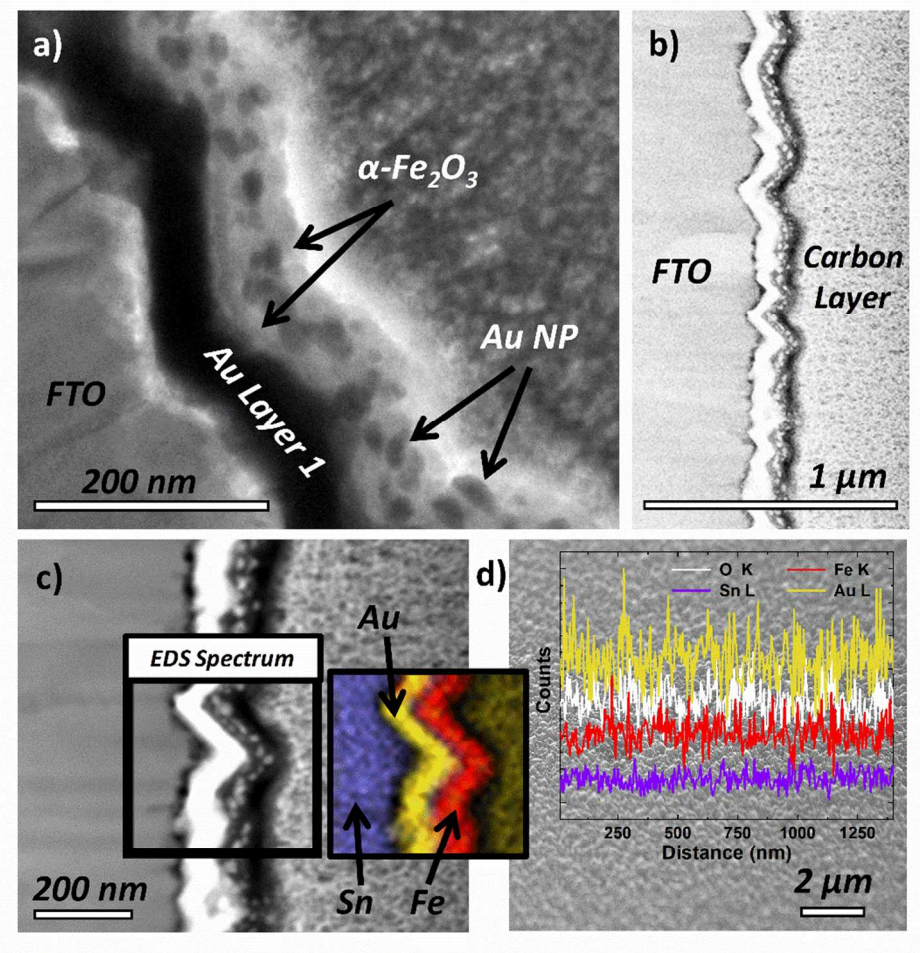
a)
α-Fe2O3
Au NP
Au Layer 1
FTO
200 nm
b)
FTO
Carbon Layer
1 µm
c)
EDS Spectrum
Au
Sn
Fe
200 nm
d)
O K
Fe K
Sn L
Au L
Counts
250
500
750
1000
1250
Distance (nm)
2 µm

Figure 4

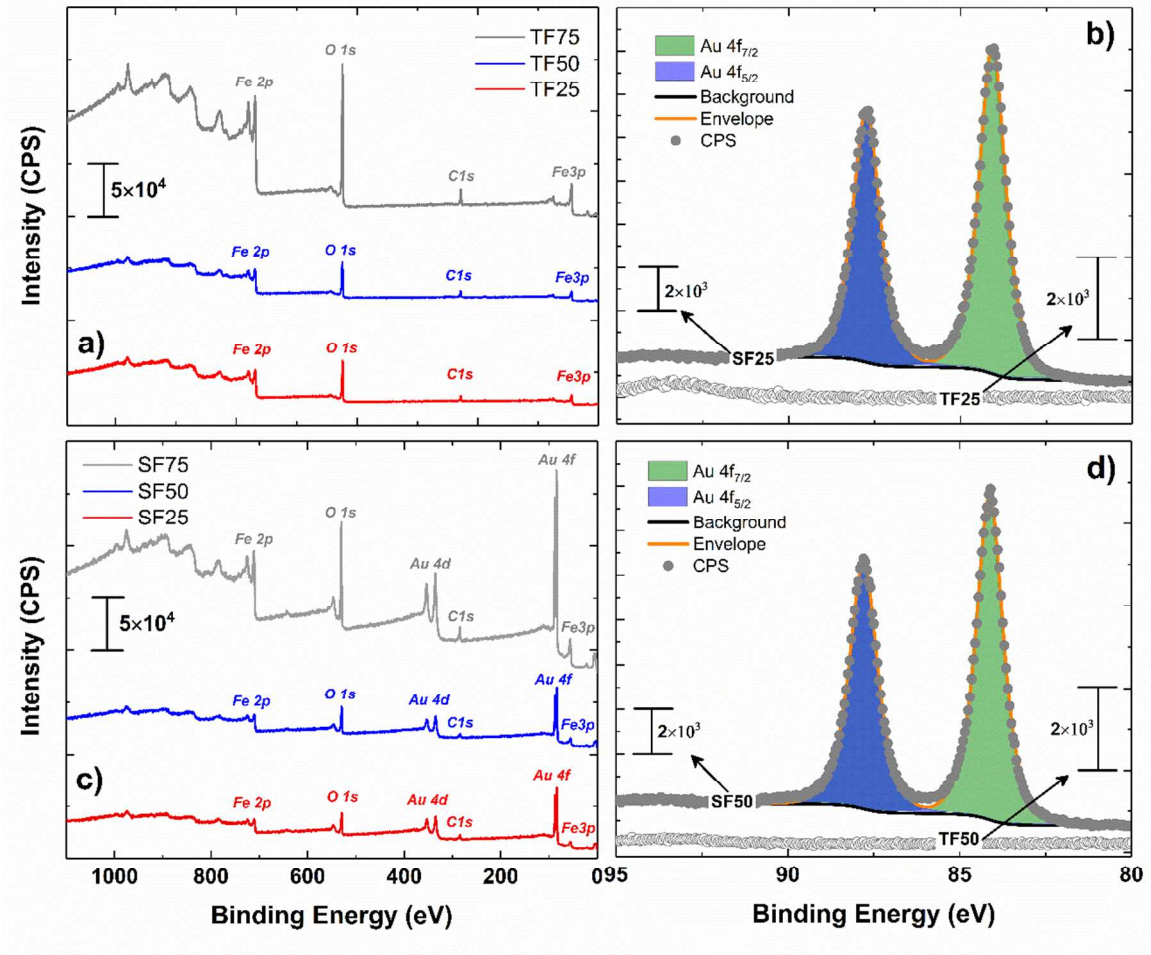
TF75
TF50
TF25
O 1s
Fe 2p
C1s
Fe3p
5×10^4
a)
Intensity (CPS)
b)
Au 4f7/2
Au 4f5/2
Background
Envelope
CPS
2×10^3
SF25
TF25
SF75
SF50
SF25
Au 4f
Au 4d
c)
d)
SF50
TF50
1000
800
600
400
200
095
90
85
80
Binding Energy (eV)

Figure 5

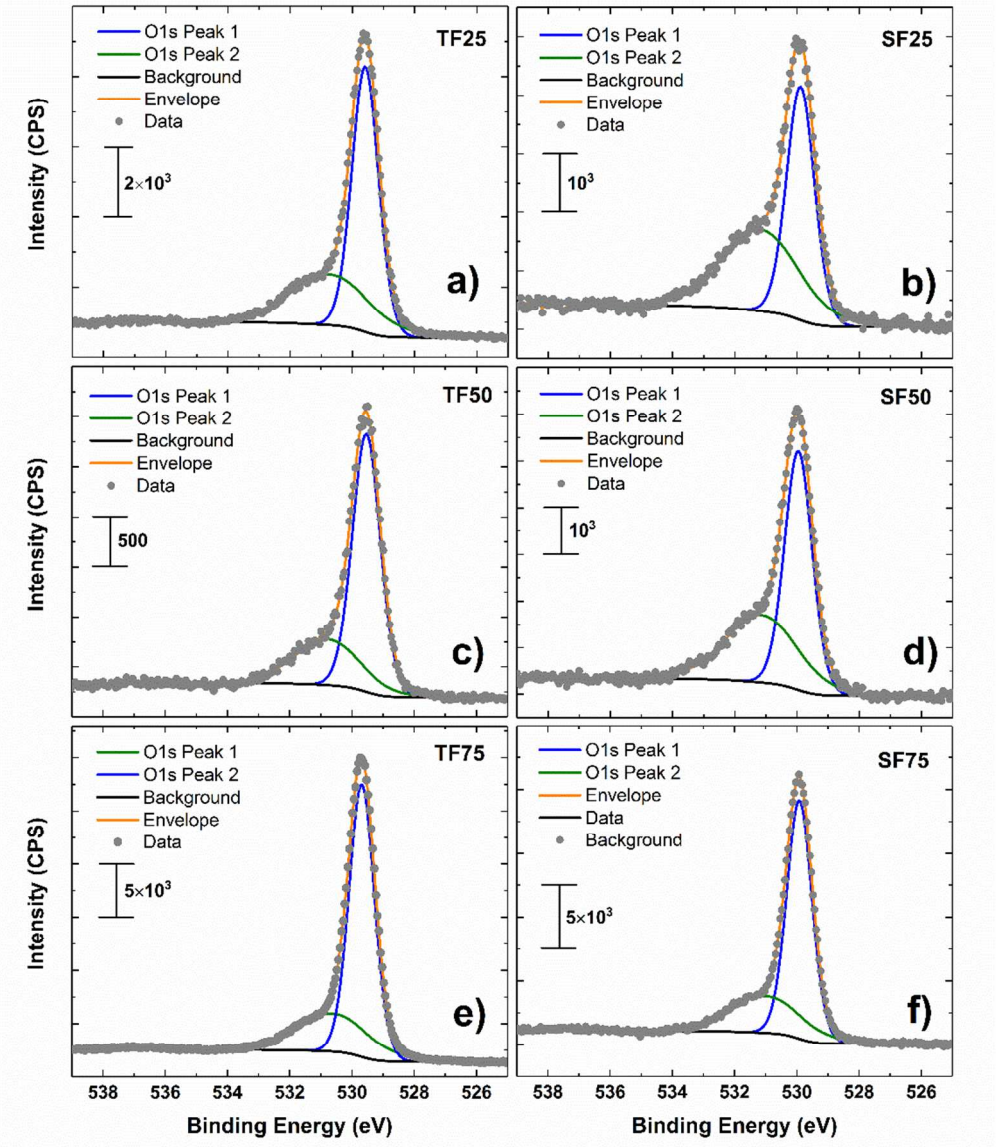
O1s Peak 1
O1s Peak 2
Background
Envelope
Data
TF25
2×10³
a)
SF25
10³
b)
TF50
500
c)
SF50
10³
d)
TF75
5×10³
e)
SF75
5×10³
f)
Intensity (CPS)
538 536 534 532 530 528 526
Binding Energy (eV)

Figure 6

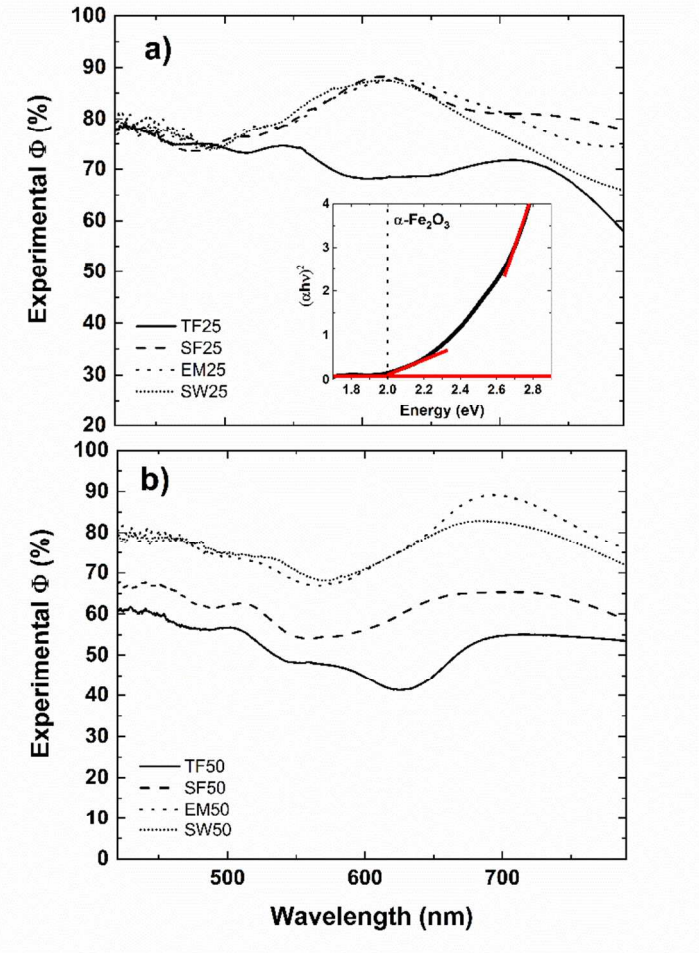
a)
b)
Experimental Φ (%)
Wavelength (nm)
TF25
SF25
EM25
SW25
TF50
SF50
EM50
SW50
α-Fe2O3
(αhν)²
Energy (eV)

Figure 7

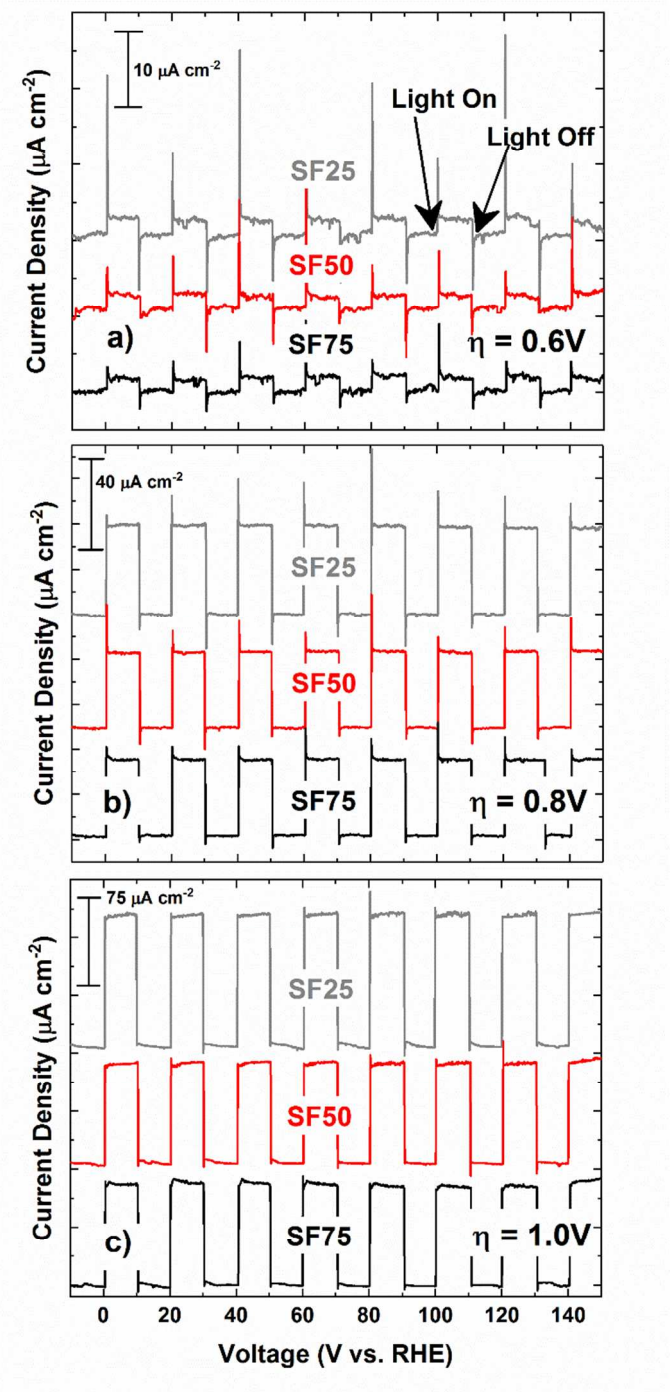
10 μA cm-2
Light On
Light Off
SF25
SF50
a)
SF75
η = 0.6V
Current Density (μA cm-2)
40 μA cm-2
SF25
SF50
b)
SF75
η = 0.8V
Current Density (μA cm-2)
75 μA cm-2
SF25
SF50
c)
SF75
η = 1.0V
Current Density (μA cm-2)
0
20
40
60
80
100
120
140
Voltage (V vs. RHE)

Figure 8

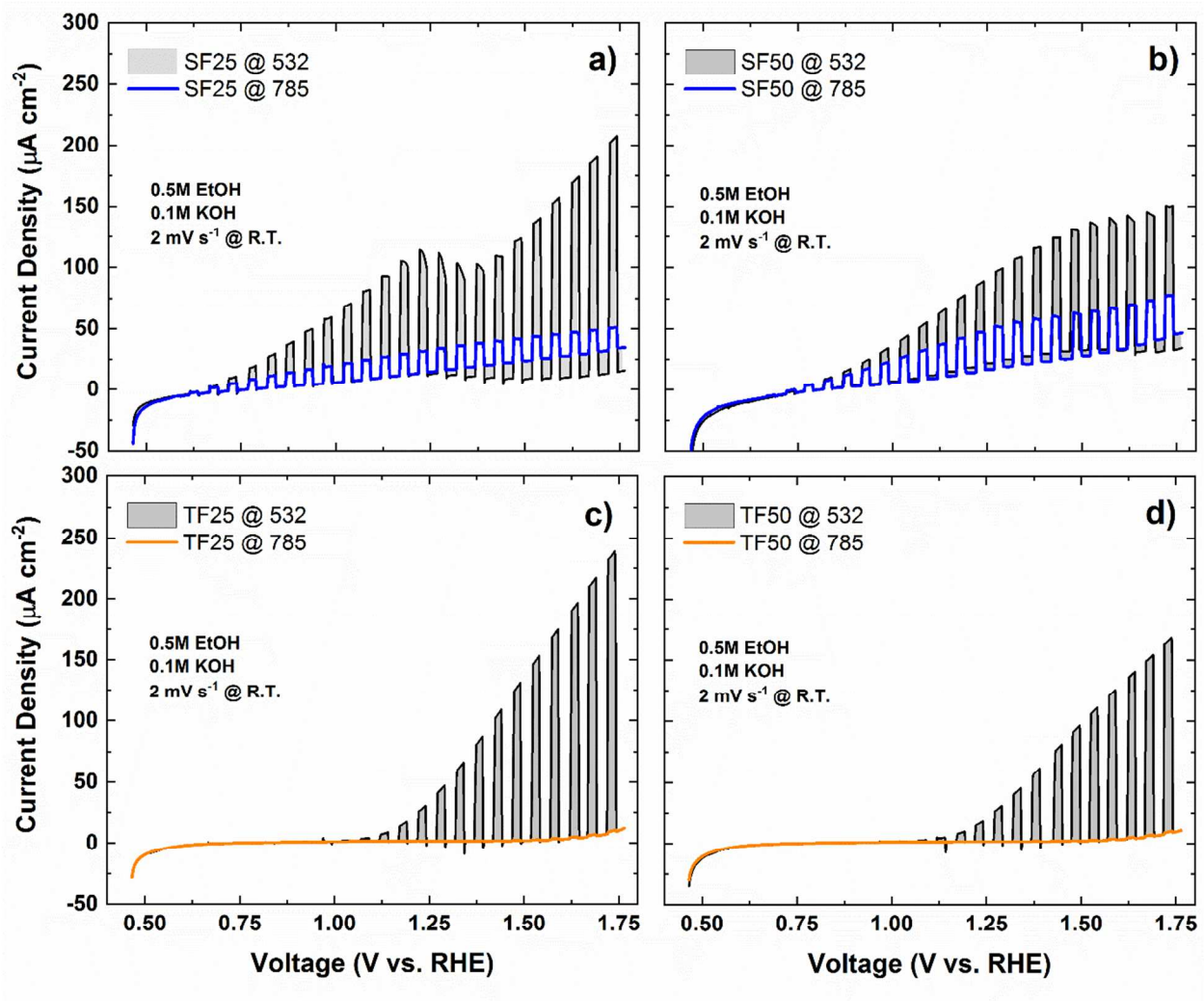
a)
SF25 @ 532
SF25 @ 785
0.5M EtOH
0.1M KOH
2 mV s-1 @ R.T.
b)
SF50 @ 532
SF50 @ 785
0.5M EtOH
0.1M KOH
2 mV s-1 @ R.T.
c)
TF25 @ 532
TF25 @ 785
0.5M EtOH
0.1M KOH
2 mV s-1 @ R.T.
d)
TF50 @ 532
TF50 @ 785
0.5M EtOH
0.1M KOH
2 mV s-1 @ R.T.
Current Density (μA cm-2)
Voltage (V vs. RHE)
300
250
200
150
100
50
0
-50
0.50
0.75
1.00
1.25
1.50
1.75

Figure 9

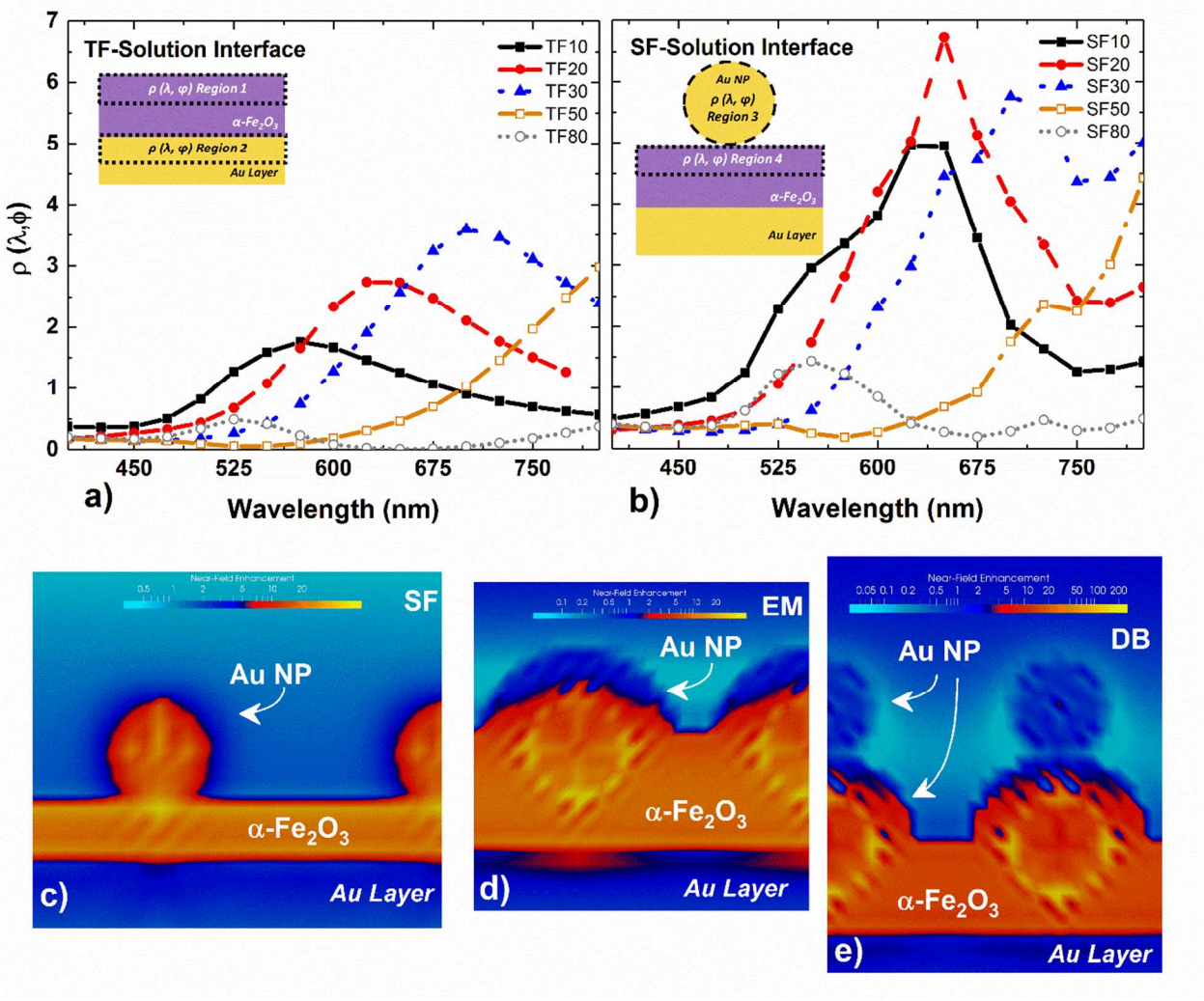
TF-Solution Interface
ρ (λ, φ) Region 1
α-Fe2O3
ρ (λ, φ) Region 2
Au Layer
TF10
TF20
TF30
TF50
TF80
ρ (λ,ϕ)
Wavelength (nm)
a)
SF-Solution Interface
Au NP
ρ (λ, φ) Region 3
ρ (λ, φ) Region 4
α-Fe2O3
Au Layer
SF10
SF20
SF30
SF50
SF80
Wavelength (nm)
b)
Near-Field Enhancement
SF
Au NP
α-Fe2O3
c)
Au Layer
EM
Au NP
α-Fe2O3
d)
Au Layer
DB
Au NP
α-Fe2O3
e)
Au Layer

Figure 10

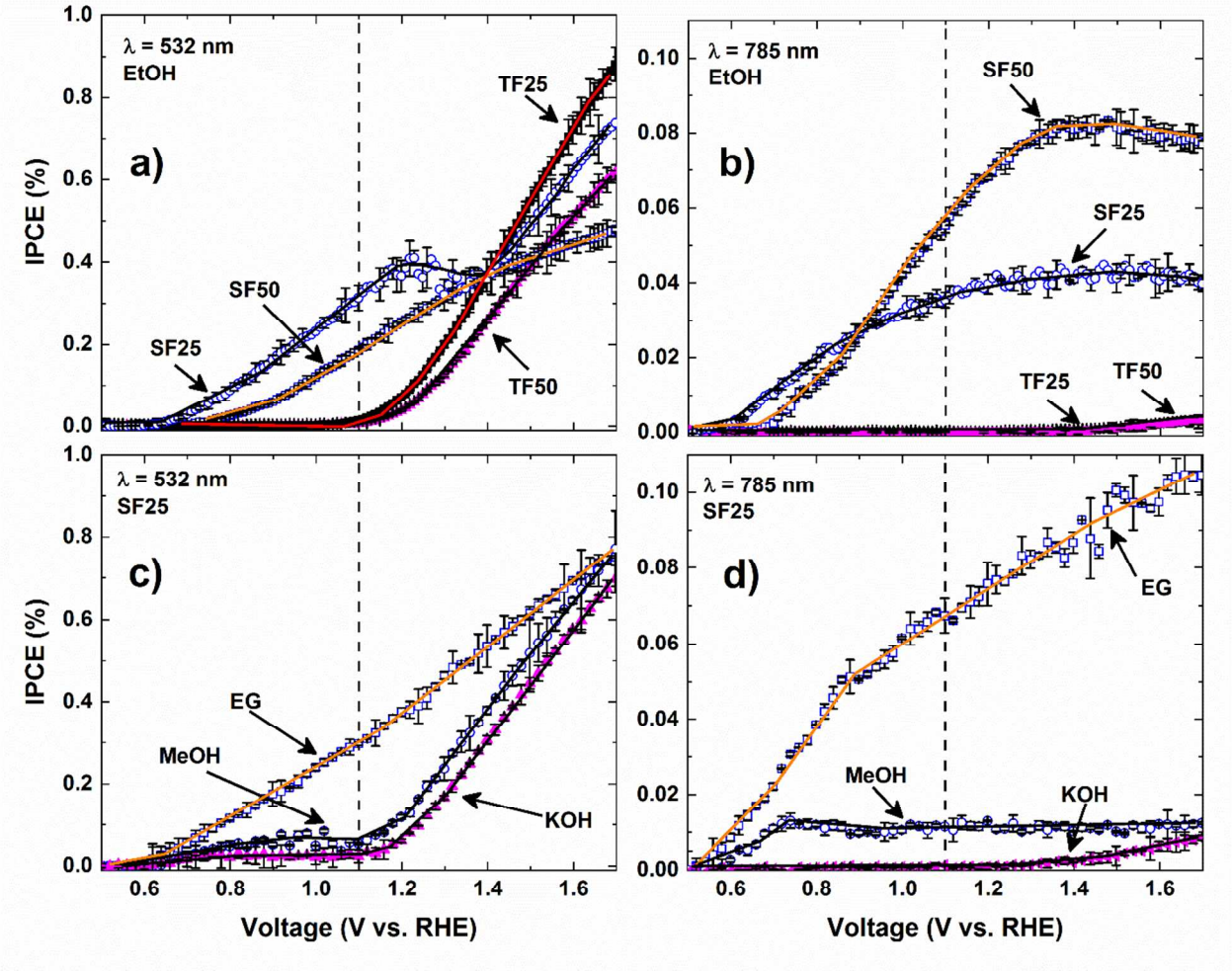
λ = 532 nm
EtOH
a)
TF25
SF50
SF25
TF50
IPCE (%)
λ = 785 nm
EtOH
b)
SF50
SF25
TF25
TF50
λ = 532 nm
SF25
c)
EG
MeOH
KOH
λ = 785 nm
SF25
d)
EG
MeOH
KOH
Voltage (V vs. RHE)
Voltage (V vs. RHE)

Figure 11

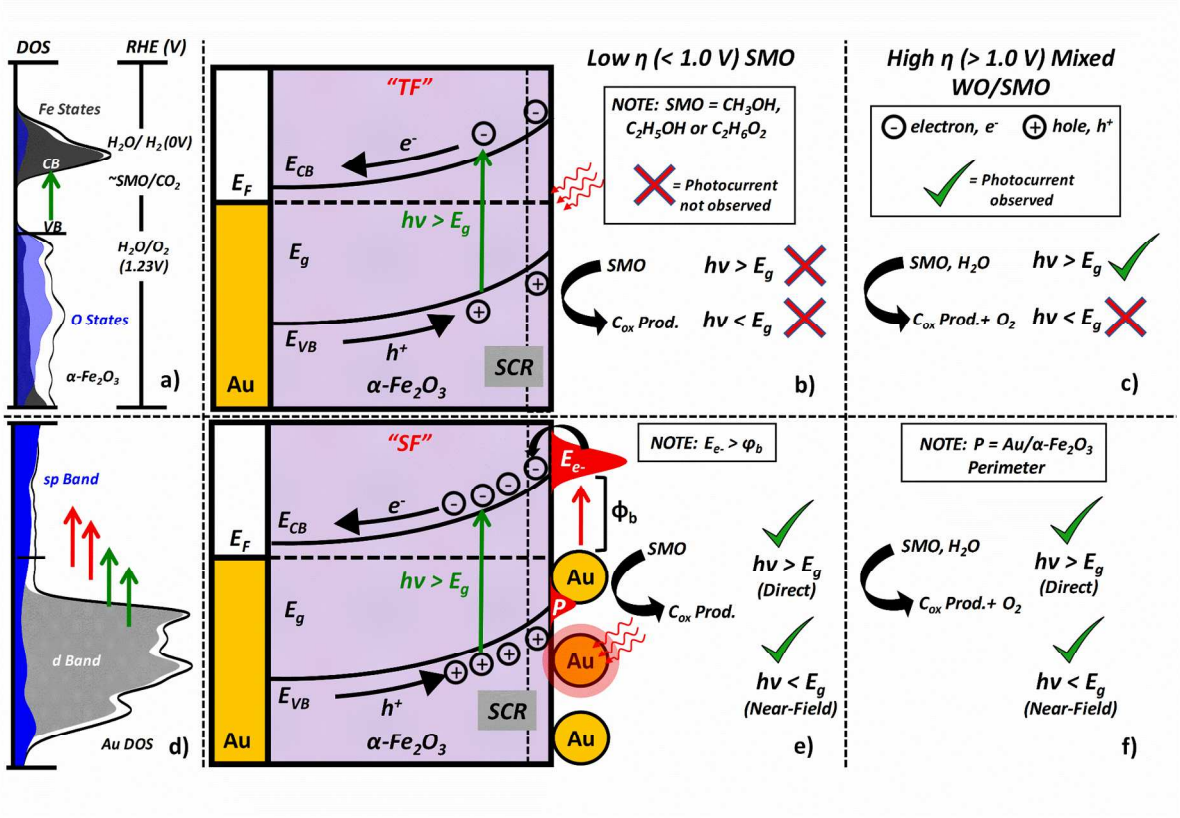
DOS
RHE (V)
Fe States
CB
VB
O States
H_2O/H_2 (0V)
~SMO/CO_2
H_2O/O_2 (1.23V)
α-Fe_2O_3
a)
"TF"
E_F
E_{CB}
e^-
$hv > E_g$
E_g
E_{VB}
h^+
Au
α-Fe_2O_3
SCR
Low η (< 1.0 V) SMO
NOTE: SMO = CH_3OH, C_2H_5OH or $C_2H_6O_2$
= Photocurrent not observed
SMO
C_{ox} Prod.
$hv > E_g$
$hv < E_g$
b)
High η (> 1.0 V) Mixed WO/SMO
electron, e^-
hole, h^+
= Photocurrent observed
SMO, H_2O
C_{ox} Prod.+ O_2
$hv > E_g$
$hv < E_g$
c)
sp Band
d Band
Au DOS
d)
"SF"
E_{e^-}
Φ_b
NOTE: $E_{e^-} > \varphi_b$
P
$hv > E_g$ (Direct)
$hv < E_g$ (Near-Field)
e)
NOTE: P = Au/α-Fe_2O_3 Perimeter
f)

Cover Art

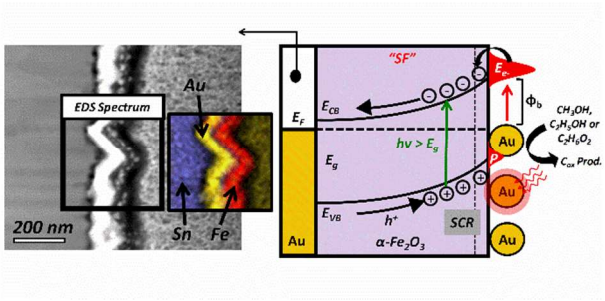

Resonantly-enhanced light-driven small molecule electro-oxidation at the hydroxyl-terminated Au/α-Fe_2O_3 Interface